Monthly Notices of the ROYAL ASTRONOMICAL SOCIETY

MNRAS **528,** 6176–6192 (2024) https://doi.org/10.1093/mnras/stae395
Advance Access publication 2024 February 9

AT2020ohl: its nature and probable implications

Rupak Roy [1]★ Samir Mandal,[2] D. K. Sahu,[3] G. C. Anupama [3], Sumana Nandi [1] and Brijesh Kumar[4]

[1]*Manipal Centre for Natural Sciences, Manipal Academy of Higher Education, Manipal 576104, Karnataka, India*
[2]*Indian Institute of Space Science & Technology, Trivandrum 695547, Kerala, India*
[3]*Indian Institute of Astrophysics, II Block Koramangala, Bangalore 560034, India*
[4]*Aryabhatta Research Institute of Observational Sciences, Manora Peak, Nainital 263001, Uttarakhand, India*

Accepted 2024 January 26. Received 2024 January 2; in original form 2023 July 12

ABSTRACT

ASASSN-20hx, a.k.a AT2020ohl, is an ambiguous nuclear transient, which was discovered in the nearby galaxy NGC6297 by the All-Sky Automated Survey for Supernovae. We have investigated the evolution of AT2020ohl using a multiwavelength data set to explain the geometry of the system and the energy radiated by it between X-ray and radio wavelengths. Our X-ray, UV/optical, and radio observations of the object jointly clarify the association of AT2020ohl with the nuclear activity of NGC6297. We detected radio counterpart of AT2020ohl 111 and 313 d after the discovery in Jansky Very Large Array X-band with flux densities 47 ± 14 and 34 ± 3 μJy, respectively. Using multiwavelength data analysis, we nullify the possibility of associating any stellar disruption process with this event. We found some evidence showing that the host galaxy is a merger remnant, so the possibility of a binary supermassive black hole (SMBH) system cannot be ruled out. The central SMBH has a mass of $\sim 1.2 \times 10^7$ $M_\odot$. We propose the accretion disc activity as the origin of AT2020ohl – it is either due to disc accretion event on to the central SMBH or due to the sudden accretion activity in a pre-existing accretion disc of the system during the interaction of two SMBHs which became gravitationally bound during a merger process. However, we also admit that with the existing data set, it is impossible to say definitively, among these two probabilities, which one is the origin of this nuclear transient.

Key words: Galaxy: disc – Galaxy: general – Galaxy: nucleus – galaxies: active – galaxies: jets – transients: tidal disruption events.

1 INTRODUCTION

The region ($\lesssim$100 pc) close to the centre of any galaxy is expected to be the harbour of various cosmic catastrophes, although it was hard to detect them observationally even a few decades ago. However, with the advent of all-sky survey programs in the recent past [e.g. Panoramic Survey Telescope and Rapid Response System, Hodapp et al. 2004; Texas Supernova Search, Quimby 2006; Palomar Transient Factory, Rau et al. 2009; Catalina Real-time Transient Survey, Drake et al. 2009; All-Sky Automated Survey for Supernovae (ASAS-SN), Shappee et al. 2014; Zwicky Transient Facility, Bellm et al. 2019], highly energetic explosions/flares have been discovered at the centres of many nearby and distant galaxies. Multichannel origin of these explosions is quite obvious. Among these energetic phenomena, if we consider only those with peak radiated power more than 10^{41} erg s^{-1}, there are three known physical processes responsible for these events. One possibility is the occurrence of luminous supernova (SN) from very massive stars located within ∼100 pc from the centre (cf., Kankare et al. 2017). The SN remnant Sgr-A East located within ∼2 pc from the centre of our Milky Way galaxy (Sgr-A*) is the nearest evidence in this regard (cf., Maeda et al. 2002 and references therein). The second possibility is the disruption of a star (roughly a solar mass) during its sufficiently close approach to the supermassive black hole (SMBH) at the centre of a galaxy. This process, which was theoretically predicted more than 40 yr ago (cf., Hills 1975; Rees 1988), although observationally found much later (cf., Komossa & Bade 1999; Gezari et al. 2009), is known as a tidal disruption event (TDE). Both possibilities are connected to disruptions of stars, although the underlying physics is completely different. The third channel is related to the accretion phenomena on to the central SMBHs of the active galactic nuclei (AGNs) and the instability associated with these processes (cf., Beckmann & Shrader 2012; Padovani et al. 2017).

However, observationally distinguishing the electromagnetic (EM) features of these nuclear transients is still a challenge. As a consequence, the nature of several newly discovered nuclear transients is debated. For example, (1) the same event has been interpreted early as an SN and later as a TDE or vice versa (e.g. ASASSN-15lh, Dong et al. 2016; Leloudas et al. 2016; CSS100217, Drake et al. 2011; Blanchard et al. 2017; ASASN-17jz, Holoien et al. 2022 and references therein), (2) a few nuclear events have simultaneously shown TDE- and AGN-like features, and in some cases detailed study could not fix their origin. These are now called as ambiguous nuclear transients (ANTs) (e.g. 1ES 1927+654/ASASSN-18el, Trakhtenbrot et al. 2019b; ASASSN-18jd, Neustadt et al. 2020), (3) a few of them did not show any significant spectral changes during their evolution (e.g. Dougie Vinkó et al. 2015; ASASSN-20hx, Hinkle et al. 2022), making their nature questionable. Some of these ambiguous phenomena may be related

★ E-mail: rupakroy1980@gmail.com, rupak.roy@manipal.edu

to the intrinsic properties of the central SMBH itself, especially associated with its dynamics and recurrent activity, which are not yet well understood. Discoveries have confirmed the presence of binary SMBH with inner separations as small as few pc (Kharb, Lal & Merritt 2017 and references therein) at the centre of a merged system. Merging (or completely merged) galaxies and/or gas accumulation processes in a single, binary (or trinary) system of galaxies is a phenomenon with a time-scale of millions of years. These are believed to be switching processes between inactive and active states of the SMBHs (e.g. Schoenmakers et al. 2001; Nandi et al. 2019 and references therein). However, for a given system, how these processes are initiated is yet unknown. Needless to say, advanced transient survey programs have provided a unique opportunity to probe the variety of SMBH triggering mechanisms and to search for their different accretion behaviours. Apart from the regular flaring activities of AGNs (which are more prominent in its Blazar subclass), long-term spectral and temporal evolutions have also been noticed in active SMBH systems (e.g. 'Changing Look' quasar, LaMassa et al. 2015). Recent observations of transients also demand the existence of 'rejuvenated' SMBHs (e.g. AT2017bgt, Trakhtenbrot et al. 2019a). While 'Changing Look' behaviours may be due to a significant change in the accretion rate on to the SMBH over a longer time-scale, or due to the dust attenuation along the line of the sight, the 'rejuvenated' scenario has been claimed to be due to a sudden matter flow in the disc of active SMBH, causing a several-order-of-magnitude rise in the ultraviolet (UV) and X-ray flux, along with the appearance of Bowen fluorescence lines. Therefore, the 'rejuvenated' SMBH scenario is expected to be observable in AGN-dominated systems.

However, the occurrence of transients due to 'rejuvenated' SMBH, in inactive or extremely mildly active systems, or association of such transient activity with the dynamics of a binary SMBH in a merged system is as yet unknown. In this work, we revisit the nuclear transient event AT2020ohl/ASASSN-20hx, which was hosted by a mildly active galaxy that might be a merger remnant. The event was extensively followed by Hinkle et al. (2022). The evolution of the transient in X-ray, near-ultraviolet (NUV), and optical wavelengths was reported, starting from −30 to 275 d relative to the maximum UV/optical brightness. The observed UV/optical light curves were fitted with TDE-models, although the shallow post-maximum decline of the light curves and non-thermal X-ray spectrum were indicators of the non-TDE origin of the object. However, it could not be characterized as a TDE, or phenomena associated with AGNs. Here we present X-ray, NUV, optical imaging and spectroscopic and radio photometric observations of AT2020ohl and the properties of its host galaxy. The NUV and optical photometric data cover about 800 d since the discovery. The pre-transient optical monitoring of the object of a similar time span is also presented in this work.

Section 2 describes the discovery and follow-up of the transient at different EM wavelengths. The nature of the host galaxy, the extinction along the line of sight, and the distance to the system are discussed in Section 3. In Section 4, the evolution of the transient in different EM wavelengths is described. The interpretations of our observational results are discussed in the Section 5 and conclusions are drawn in the same section.

2 AT2020OHL – DISCOVERY AND FOLLOW-UP

AT2020ohl/ASASSN-20hx was discovered by the ASAS-SN survey (Brimacombe et al. 2020) on UT 2020-07-10.34 at $g \sim 16.7$ mag at the centre of the nearby ($z = 0.0167$) galaxy NGC 6297. It was initially classified as a TDE (Hinkle et al. 2020), and further analysis of the early Neil Gehrels *Swift*[1]/X-ray Telescope (XRT) observations suggested it as a hard X-ray TDE candidate with a spectral index roughly between 2.2 and 2.6 (Lin 2020). The transient was extensively followed by Hinkle et al. (2022), mainly in the X-ray, NUV, optical bands, and mid-IR in a few epochs. They also analysed the early data observed by *TESS*[2] during the rising phase of the transient. The rise in the *TESS* data was estimated to be on JD $= 2459023.3^{+0.8}_{-0.6}$ (Hinkle et al. 2022), compared to the discovery date i.e. JD = 2459040.8, 17.5 d later the initial explosion. This value is also consistent with the limit of non-detection by Brimacombe et al. (2020). In this work, we use JD = 2459023.3 as the epoch of explosion (t_0), and all the phases are measured with respect to t_0.

Although the early bluish spectral energy distribution (SED) of the source, starting from UV to optical, along with X-ray detection, supported its TDE nature (as discussed in the subsequent sections, and also by Hinkle et al. 2022), the overall behaviour of AT2020ohl was not like canonical TDEs. Therefore detailed multiwavelength follow-ups and analyses were necessary. To achieve this goal, we performed targeted observations of the transient in the X-ray, UV, optical, and radio bands. A brief overview of our observations has been discussed below.

2.1 Optical spectroscopic observation

Long-slit low-resolution optical spectra (0.4–0.8 μm) were collected from the 2m Himalayan Chandra Telescope (HCT) at seven epochs, viz. 2020-08-31, 2020-09-08, 2020-09-29, 2020-10-16, 2020-12-02, 2021-03-27, and 2021-10-19. A journal of spectroscopic observations is given in Table A1. The data were reduced in the IRAF[3] environment. Bias and flat-fielding were performed on all the frames. Cosmic-ray rejection was done using the Laplacian kernel detection method (van Dokkum 2001). The instrumental resolution (full width at half-maximum) of these spectra, as measured from the [O I] λ5577 emission skyline, was found to lie between 6 and 10 Å (∼322–510 km s^{-1}). Flux calibration was done using standard spectrophotometric star fluxes from Hamuy et al. (1994). SDSS survey[4] provides a low-resolution pre-explosion spectrum with moderate signal-to-noise ratio (SNR) of the centre of NGC 6297. These archival data of the host are used in our analysis.

2.2 Jansky Very Large Array radio observation

Prior to AT2020ohl, the centre of NGC6297 was not detected in radio wavebands. We analysed available archival radio data from the FIRST,[5] NVSS,[6] and GB6[7] radio sky surveys. The host was detected neither in the 1.4 GHz NVSS nor FIRST surveys (with limiting sky-rms 0.45 and 0.15 mJy beam^{-1}, respectively), nor in the 5 GHz GB6

[1] *Neil Gehrels Swift Gamma-ray Burst Mission* (hereafter *Swift*) (Gehrels et al. 2004).
[2] Transiting Exoplanet Survey Satellite (Ricker et al. 2015).
[3] IRAF stands for Image Reduction and Analysis Facility distributed by the National Optical Astronomy Observatory, which is operated by the Association of Universities for Research in Astronomy, Inc., under a cooperative agreement with the National Science Foundation.
[4] https://skyserver.sdss.org/dr12/en/tools/chart/navi.aspx
[5] FIRST stands for Faint Images of the Radio Sky at Twenty-cm (Becker, White & Helfand 1995).
[6] NVSS stands for The NRAO VLA Sky Survey (Condon et al. 1998).
[7] GB6 is the Green Bank telescope 4.85 GHz sky survey (Gregory et al. 1996).

survey (limiting sky-rms 3 mJy beam^{-1}). We did not find any pre-transient radio emission in the 3 GHz radio sky survey VLASS[8] as well (limiting sky-rms 0.12 mJy beam^{-1}).

Motivated by the detection of the X-ray counterpart of AT2020ohl, we observed the field using Jansky Very Large Array (JVLA) at three epochs in two frequencies – *X* band (8–12 GHz) and *C* band (4–8 GHz). The X-band observations were done on 2020 October 29 (proposal code VLA/20B-427) and 2021 May 19 (proposal code VLA/21A-420) using the B-array and D-array configurations, respectively. In *C* band, it was done only in the D-array configuration on 2021-05-24 (VLA/21A-420). The raw data were calibrated using the standard VLA pipeline tool[9] which is based on CASA.[10] After calibration the target data were extracted using the task `split`, and then imaged by `tclean`. The JVLA Synthesized Beam width in the B-array in *X* band is 0.6 arcsec, whereas in D-array, they are 7.2 and 12 arcsec for the *X* band and *C* band, respectively. A radio counterpart was detected from NGC 6297 in all of our observations. Details of the radio observations are given in Table A2.

Due to its higher spatial resolution, the X-band observation on 2020 October 29 revealed two radio sources near the centre of NGC6297 – a central component with a second radio knot at a separation of 1.5 arcsec from the centre of the galaxy. This angular separation is extremely small compared to the projected dimension (of major axis.[11]) of the host (Makarov et al. 2014)[12], which is roughly 38 arcsec. However the aforementioned high-resolution radio observation was inadequate to distinguish the transient from those two radio counterparts at the centre of NGC 6297. Noteworthy, the optical spectra (acquired using a slit of width 1.5 arcsec) also contain both host and transient spectra. Therefore the present data set cannot spatially resolve the transient from its host's centre. Nevertheless, since the X-ray counterpart of AT2020ohl was detected by *Swift*/XRT, high-resolution X-ray imaging of the field using *Chandra* X-ray observatory[13] was done to mark the transient position precisely.

2.3 *Swift*/UVOT observation

Swift/UVOT data have also been used to study the NUV and optical counterparts of the transient.[14] Early *Swift*/UVOT observations (till 275 d post-maximum) were reported by Hinkle et al. (2022). In this work, we have compiled the *Swift* NUV data till ∼800 d post-maximum. The public *Swift* data are available on the website of 'Heasarc'. The *Swift* data were reduced using the standard pipeline available in the HEASOFT software package.[15] UVOT observations at each epoch were conducted using one or several orbits. To improve the SNR in a given band at a particular epoch, all orbit data of that corresponding epoch have been co-added using the HEASOFT routine `uvotimsum`. The routine `uvotdetect` is used to determine the correct position of the transient (which is consistent with the ground-based optical observations). We used the routine `uvotsource` to perform aperture photometry. For source extraction, a small aperture of radius 3.5 arcsec was used to minimize the host contamination, while an aperture of radius 50 arcsec was used to determine the background.[16] The host-subtracted UVOT photometry is presented in Table A3.

2.4 *Swift*/XRT observation

Swift XRT operates in the energy range 0.3–10 keV (Burrows et al. 2005). XRT monitored the source AT2020ohl over 800 d, starting from 2020 July 19 (MJD 59049). Like NUV observations, we have also used the publicly available *Swift*/XRT data of this event till ∼800 d post-maximum, while only the initial ∼275 d XRT observations were reported by Hinkle et al. (2022). The source was X-ray-faint, and XRT observed the source in photon counting mode. In this study, we considered all observations with an exposure time greater than 700 s to achieve a good SNR. The XRT data reduction followed the standard procedure.[17] We ran `xrtpipeline` to generate the Level 2 products. We select a circular region having a 20-pixel radius around the source and a larger circle with a radius of 50 pixels as the background region. No pile-up is detected in the source data. We use `XSELECT` to create the source and background spectrum. The `xrtmkarf` tool with the source spectrum and exposure map is used to generate the ancillary response function file for each observation. We use the response files (RMF) from the CALDB version 20220803.[18] All the bad channels are ignored. We group the source spectrum with 'group min 1' to ensure at least one count per bin and use `cstat` in XSPEC for spectral modelling. The details of the XRT observations are tabulated in Table A4.

2.5 *Chandra* X-ray observation

We observed the AT2020ohl with the *Chandra* X-ray space telescope on 2021 April 16, using the High Resolution Camera for Imaging (HRC-I) instrument to obtain an image with a high spatial resolution (∼0.4 arcsec). This observation was also necessary to localize the non-thermal X-ray emission and its association with the possible radio counterparts.

2.6 Other archival data

The transient occurred at the centre of the host. Therefore, it is essential to remove the host contribution from the observed flux, to

[8] VLASS stands for VLA Sky Survey (Lacy et al. 2020).
[9] https://science.nrao.edu/facilities/vla/data-processing/pipeline
[10] https://casa.nrao.edu/
[11] Noteworthy, the length of the major axis of a galaxy, projected on the sky-plane, is its length measured at the isophotal level 25 mag arcsec^{-2} in the *B* band.
[12] http://leda.univ-lyon1.fr
[13] https://chandra.harvard.edu/
[14] Jason T. Hinkle is the Principal Investigator of all of the *Swift*/UVOT and XRT observations. The raw public data of the entire observation are available in the Heasarc website (https://heasarc.nasa.gov/).
[15] https://heasarc.nasa.gov/lheasoft/
[16] 'Aperture-correction' has been applied to the count rates to correct for the missing counts while computing the photometry. It is possible that when multiple photons are coincident on the same area of the UVOT detector, it does not count all the photons. This effect is known as 'coincidence loss'. The `uvotsource` routine makes the necessary correction to compensate for the 'coincidence loss' effect. Noteworthy, to remove the host contamination from the measured NUV-optical magnitudes, pre-flare photometric and spectroscopic data of the galaxy taken from *GALEX* and SDSS have been used. UVOT also imaged the host in *uvw1* and *U* bands on 2018-07-27 and 2019-06-21, much before the transient happened, as part of the Swift Gravitational Wave Galaxy Survey (SGWGS, Evans et al. 2012). These UVOT images were also used to compute the host magnitudes in those bands, using an identical source region. The method adopted to measure the central magnitudes of the host in different UVOT bands is discussed in Section 3.
[17] https://www.swift.ac.uk/analysis/xrt/
[18] https://heasarc.gsfc.nasa.gov/docs/heasarc/caldb/data/swift/xrt/index.html

compute the actual flux of the transient at different epochs. We used the pre-explosion archival SDSS spectrum of the host centre (Smee et al. 2013), which was acquired much before the occurrence of AT2020ohl. We have also used the archival photometric data from the SDSS survey to compute the central flux of the host. The procedure is described in Section 3. The ATLAS sky survey (Tonry et al. 2018) observed the field more than 800 d before the event and continued the monitoring afterword. We use ATLAS forced-photometry on the host-subtracted frame[19] where there are 5σ detections[20] (see Section 4.1).

3 THE HOST – NGC6297

Morphologically, the host is an S0 galaxy[12]. The absence of star-forming lines and AGN lines in the pre-transient archival SDSS spectrum indicate that the AGN activity in this galaxy has been quenched (or at a very low level). This is also consistent with its X-ray faintness in the pre-transient ROSAT[21] X-ray observations. However, analysis of pre-transient *Swift*/XRT observations reveal a faint X-ray luminosity $\sim 3.4 \times 10^{41}$ erg s^{-1}, which points to the existence of a low-luminous AGN (LLAGN) at the centre of NGC6297 (Hinkle et al. 2022 and references therein).

S0 galaxies are found in various environments that indicate multiple pathways of their formation (e.g. Deeley et al. 2020). Various possible channels have been proposed for their formation – either through gas stripping of spirals inside dense galaxy clusters (e.g. Quilis, Moore & Bower 2000) or by merging of disc-dominated galaxies (e.g. Querejeta et al. 2015) or due to merging of compact ellipticals with their gas-rich irregular companions (Diaz et al. 2018). There are also observational evidence suggesting that galaxies with 'bars/lenses' make a significant contribution to the formation of S0 galaxies, which is difficult to explain with these formation mechanisms (Laurikainen et al. 2009).

We used the SDSS *r*-band image to measure the surface brightness properties of NGC6297. The left panel of Fig. 1 shows the radial profile of the *r*-band intensity of the galaxy in terms of mag arcsec^{-2} found by fitting concentric isophotes. The outermost isophote is at a distance of $\sim$12 kpc from the centre of the galaxy. The surface brightness of massive galaxies is commonly modelled with two components – a Sersic profile for the central bulge and an exponential profile for the disc (Graham & Driver 2005). We found that along with the Sersic profile, two exponential profiles are required to model the surface intensity distribution of NGC6297. The value of the reduced chi-square (χ^2) for the 'Sersic and 'single-exponential' profile is 12.3, while that for the 'Sersic and double-exponential' profile is 0.9. This implies that the disc of NGC6297 may have two components – an inner disc with a steeper intensity profile and an outer disc with shallower intensity profile. The presence of an extended disc with multiple components probably supports the merging scenario as the origin of the host of AT2020ohl (see Section 5).

To estimate the true transient flux (and hence the magnitude) in UVOT bands, the flux of the host at different UVOT bands is needed. However as the system remained variable over a long time-scale in the post-flare epochs, we computed synthetic magnitudes of the host-centre from the archival data. The archival SDSS spectrum (re-calibrated using the 3.5 arcsec aperture-photometry of the host-centre) and the SED produced from the archival *GALEX* measurements were used. This is shown in the right panel of the Fig. 1.[22] The synthetic magnitudes of the host-centre, in the UVOT *uvw2, uvm2, uvw1, U, B,* and *V* bands, which correspond to flux within an aperture of radius 3.5 arcsec are, respectively, $\sim$18.28, $\sim$18.75, $\sim$17.79, $\sim$17.39, $\sim$16.05, and $\sim$15.00 mag.[23] For the rest of the work, we use these magnitudes as the measures of NUV-optical fluxes of the quiescent galaxy.

3.1 Distance and extinction towards NGC6297

The spectrum of NGC6297 does not have any strong emission lines. The redshift (z) of the host computed from its narrow Balmer lines is $\sim$0.01671 (Adelman-McCarthy et al. 2006). This corresponds to a luminosity distance (D_L) of $\sim$72.9 Mpc, adopting a standard cosmology[24] corresponding to a distance modulus (μ) $\sim$34.3.

Estimation of the reddening towards the centre of NGC6297 (particularly the contribution due to the host) is non-trivial. The Galactic contribution derived from Schlafly & Finkbeiner (2011) is 0.0203 $\pm$ 0.0011. The inset of the right panel of Fig. 1 shows the region around the Na I D$\lambda\lambda$5890, 5896 absorption lines in the SDSS spectrum of the host. The lines from the Milky Way and host have been marked with cyan and reddish regions. Impression of Na I D doublet in the spectrum has been considered as a moderate tracer of reddening towards the line of sight over the last couple of

[19] https://fallingstar-data.com/forcedphot/

[20] ATLAS usually observes in a quad, i.e. four images of the same sky area during a given night. To improve the SNR, the fluxes of the object obtained from the host-subtracted photometry in a given night have been stacked. Further, only the 5σ detections have been considered for this analysis, and corresponding AB magnitudes have been computed.

[21] https://www.dlr.de/content/en/articles/missions-projects/past-missions/rosat/rosat-mission.html

[22] To calculate the central flux of the host, the pre-flare images of NGC6297 in FUV and NUV bands (from *GALEX* observation), and in NUV-optical bands (from UVOT and SDSS observations) have been used. As discussed in Section 2.3, for UVOT data analysis, an aperture of radius of 3.5 arcsec has been used. To calculate the central flux of the host in UVOT-filters within an aperture of 3.5 arcsec radius, first we re-calibrated the observed flux density of the pre-flare SDSS spectrum of the centre (acquired using optical fibre of radius 1.5 arcsec) with respect to the magnitudes of the host-centre in SDSS *g* (15.85 $\pm$ 0.05 mag) and *r* (15.07 $\pm$ 0.04) bands, computed from the pre-flare SDSS images taking an aperture of radius 3.5 arcsec. Here, we have assumed that the relative flux calibration of the SDSS-spectrum is correct. The original (in blue) and the re-calibrated (in green) SDSS spectra are shown in the right panel of Fig. 1. Further, to construct the SED of the host-centre in UV wavelengths, pre-transient observations from *GALEX* (in FUV and NUV bands) and *Swift* (in *uvw*1, *U* bands) have been used and computed by fitting a lower order (order 3) polynomial to these pre-transient UV data. It is shown with the magenta line in the figure. The magnitudes of the host centre are, respectively 20.85 $\pm$ 0.29, 18.89 $\pm$ 0.07, 18.58 $\pm$ 0.20, and 17.56 $\pm$ 0.01 in FUV, NUV, *uvw*2, and *U* bands. After constructing the entire re-calibrated UV-optical spectrum of the host-centre (i.e. magenta+green lines in the above-mentioned figure), we have computed the synthetic magnitudes of the host centre (that corresponds to the flux-density within an aperture of 3.5 arcsec radius) in *Swift*/UVOT filters (viz. *uvw*2, *uvm*2, *uvw*1, *U*, *B*, *V*) using their corresponding response curves and following equation (1) of Koornneef et al. (1986).

[23] Hinkle et al. (2022) computed the synthetic magnitudes of the host centre considering an aperture of radius 5 arcsec and using the synthetic spectrum produced from the code FITTING AND ASSESSMENT OF SYNTHETIC TEMPLATES (FAST, Kriek et al. 2009). We have reproduced their results by taking an aperture of radius 5 arcsec. However, in this work, to reduce the host contamination from the beginning, we have used 3.5 arcsec aperture to extract the source, and applied aperture correction.

[24] Throughout this paper the cosmology model with $\Omega_M = 0.3$, $\Omega_\Lambda = 0.7$, and $H_0 = 69.6$ km s^{-1} Mpc^{-1} has been assumed (Wright 2006).

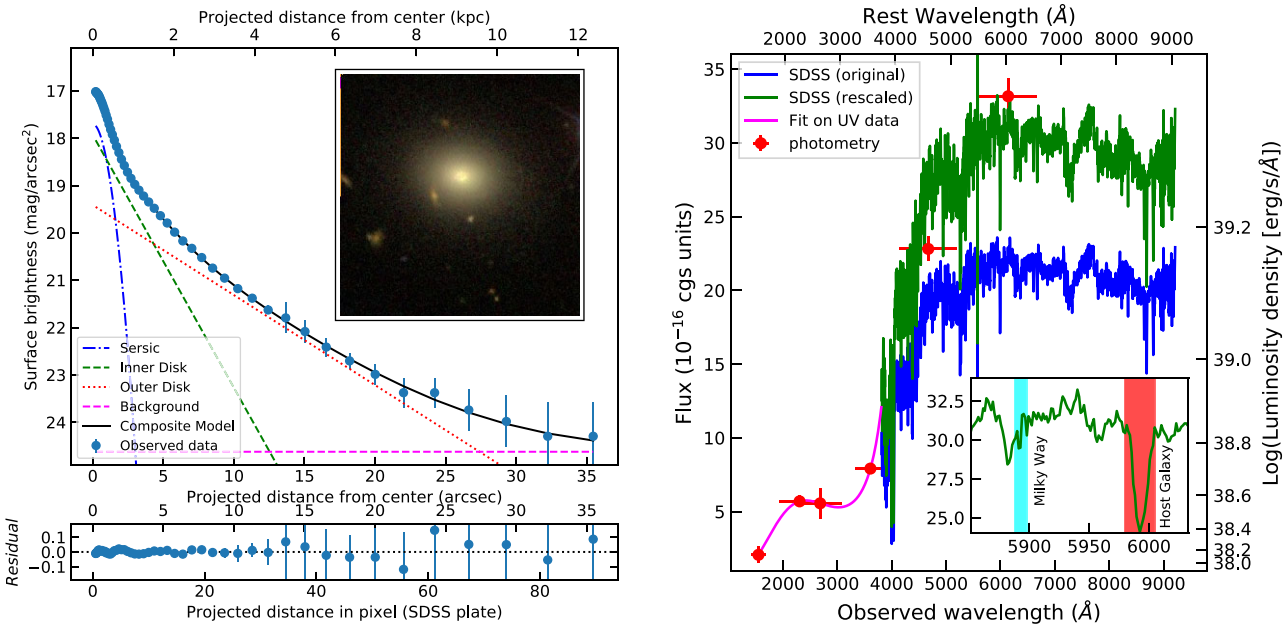

Figure 1. NGC6297 – the host of AT2020ohl. Left panel: surface brightness of the galaxy as a function of radius (blue points). The black curve shows the resulting model fit for the SDSS *r*-band data from the combination of Sersic (blue dash–dotted line), inner exponential-disc (green dash line), and outer exponential-disc (red dotted line) profiles. Th dot–dashed purple line is the background, while the inset shows an ∼1.5 arcmin × 1.5 arcmin SDSS colour composite image of NGC6297. Right panel: the UV-optical spectrum of the centre of NGC6297. The blue spectrum shows the original flux-calibrated SDSS observation (using an optical fibre of radius 1.5 arcsec). The green spectrum is obtained after re-scaling the SDSS spectrum with respect to the central '*g*' and '*r*' band fluxes of the host computed within an aperture of radius 3.5 arcsec (red points). These photometric measurements have been done on the pre-flare SDSS images. The magenta curve is the low-order polynomial fit over the available pre-flare UV data. The inset shows the region around the Na I Dλλ5890, 5896 doublet in the calibrated observed spectrum. The cyan shaded region shows the contribution due to the Milky Way, while the red region marks that due to the host galaxy.

decades (e.g. see Barbon et al. 1990; Richmond et al. 1994; Turatto, Benetti & Cappellaro 2003; Poznanski, Prochaska & Bloom 2012), although recent studies suggest a significant deviation from the previously proposed correlations, particularly using low-resolution spectra (e.g. see Phillips et al. 2013). The equivalent width (EW) of the Na I D doublet due to Milky Way is ∼0.1795 Å, which corresponds to a reddening of ∼0.04 according to Barbon et al. (1990), and $0.023^{+0.005}_{-0.004}$ according to Poznanski, Prochaska & Bloom (2012). Note that both measurements are consistent with the above-mentioned value of the Galactic reddening. Therefore, the average Galactic reddening along the direction of the transient is ≈0.028. Na I D absorption dip of the host is more prominent (although the components of the doublet are unresolved) than that of Milky Way. The EW of this unresolved line is 2.63 ± 0.22 Å (the error in EW is estimated using equation 6 of Vollmann & Eversberg 2006). This corresponds to a reddening from the host galaxy 0.66 ± 0.05 according to Barbon et al. (1990) and to Poznanski, Prochaska & Bloom (2012) corresponding value of reddening is ∼16, which is essentially infeasible.

Therefore, in this work, we presume that the contribution of the host in reddening towards the centre of NGC6297 is negligibly small. This is mainly supported by the following attributes: (a) the transient remains highly luminous in the NUV for a long time (see Section 4), (b) the host is a S0 galaxy, therefore the star formation in its centre may have been quenched, causing a very less abundance of dust along the centre of the host. Therefore, considering only the Galactic absorption, the total reddening towards the transient is $E(B-V) \approx 0.028$. This implies the total extinction towards AT2020ohl in *V* band is $A_V \approx 0.09$ mag, adopting the uniform value of total-to-selective extinction ratio (R_V) = 3.1 of the Milky Way.

4 EVOLUTION OF AT2020OHL

Using the high-cadence pre-transient data from *TESS* Hinkle et al. (2022) found a smooth rise in flux from the pre-transient to the transient state, following a power law with temporal index ∼1.05. In this work, we will mainly focus on the post-maximum evolution of AT2020ohl. Fig. 2 shows the X-ray, UV, and optical light curves of the transient. The red and blue vertical lines mark the onset of the event (from *TESS* observation) and the first detection reported by the ASAS-SN survey (see Section 2).

4.1 UV-optical light curve

Flat/quasi-flat light curves are prominent during the first 120 d in all UVOT-bands, followed by a gradual decay until ∼+400 d in the rest frame of the transient. Assuming a power-law decay of the flux with time ($f \propto t^{-\alpha}$), two distinct decay profiles were seen before and after +120 d in each light curve. Before +120 d, the temporal index (α_1) remained almost constant in all UVOT bands (0.07 ± 0.01 in *uvw2*, to 0.01 ± 0.01 in *V* band). Between 120 and 400 d, a steeper decay (with index α_2) is observed. It is more prominent in the NUV bands, with a larger value of α_2 (0.41 ± 0.02), while shallower in *U* band (roughly 0.3) and even shallower in *B* and *V* bands (roughly 0.1). Beyond +400 d, a shallow rise is seen for all of the NUV bands for the next 150 d followed by a decay until +700 d. In the *B* and *V* bands, the corresponding variations are almost negligible, although a decay of the *U*-band flux beyond +550 d is also noticeable.

The left panel of Fig. 3 shows the ATLAS forced-photometry of the centre of NGC6297, performed on the host-subtracted images in the ATLAS Orange (o) and Cyan (c)-bands and covering a timespan

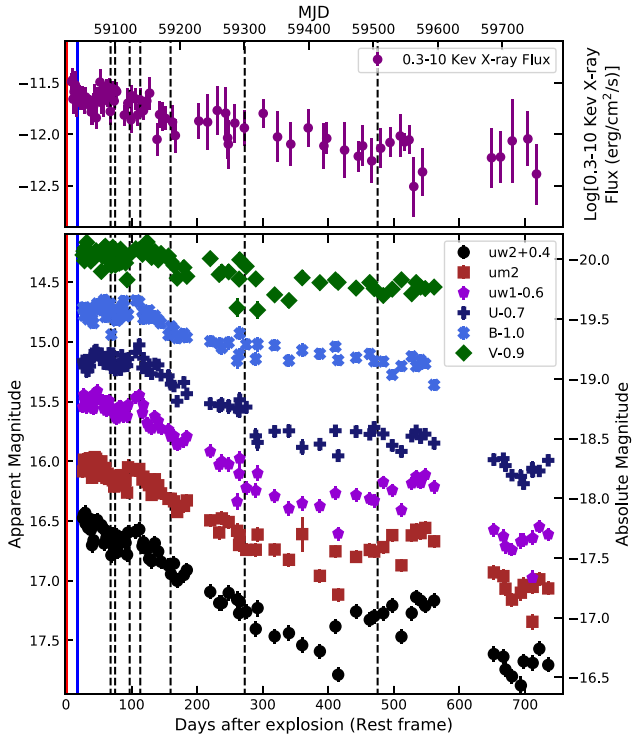

Figure 2. The X-ray, UV, and optical light curves of AT2020ohl. The lower panel shows the UV-optical light curve of the transient. All the observed magnitudes of the transient have been obtained by subtracting the host central flux from the measured fluxes of the central region at different epochs as detailed in Section 3. Variations in magnitudes in small and large time-scales are noticeable. The upper panel shows the corresponding variations in the X-ray fluxes. The red and blue vertical lines, respectively, mark the last non-detection and first detection reported by ASASSN. Note that the last non-detection was noticed ∼2 d before the epoch when the first rise was observed by *TESS* (Section 2) The black dashed vertical lines mark the epochs when HCT spectroscopic observations were performed.

from ∼−800d to +800d with respect to the onset of the event (i.e. t_0). Prior to that, fluctuations around the median of 19 mag are noticeable in both ATLAS bands. However, from these data, it would be exaggerated to say that those fluctuations are precursors of AT2020ohl. Nevertheless, it is noteworthy that on MJD = 59000.4 (i.e. 22 d before the onset of the event in the source frame), the object became brighter than the median by 0.7 mag in the o band. This flux enhancement is within 2σ from the median value (where standard deviation for the pre-event o-band measurements is ∼0.5 mag). The trend in the enhancement of flux in the o band during that period is more prominent in 3σ clipping analysis and, to some extent, is also noticeable in *TESS* observations (see fig. 4 of Hinkle et al. 2022). This may be a precursor of AT2020ohl. However, a rise in the c band was not observed in either of the 5σ or the 3σ clipped photometry. So, if it is indeed a precursor of AT2020ohl, the corresponding spectrum must be very reddish.

On the other hand, beyond +400 d a little rise in both o-band and c-band fluxes can be seen. As the host galaxy is faint in NUV and *U* bands, a flux enhancement during that period has also been found from the analysis of *Swift* data. The enhancement in NUV is noticeably higher than other optical bands.

A close inspection of the first 120 d of photometric evolution after the peak reveals significant variation in the UV-optical light curves (right panel of Fig. 3). The solid lines with periodicity ∼11 d are overplotted with the data. Similar behaviour has also been noticed in X-ray light curve (with a periodicity of ∼8 d) during this timespan. However, due to the lack of high-cadence data with regular intervals, we cannot perform any quantitative analysis to conclusively establish the periodic variation in the light curves.

4.2 X-ray light curve and spectrum

The upper panel of Fig. 2 shows the X-ray light curve. Like UVOT data, all of the orbit data of a given *Swift*/XRT observation were stacked to improve the SNR. We fit the individual, as well as the time-averaged X-ray spectra with the `ztbabs*powerlaw` model with a line-of-sight Hydrogen column density $n_H = 1.3 \times 10^{20}$ cm^{-2}. The photon index of the time-averaged X-ray spectrum is ∼2.1 (see the right panel of Fig. 4). From the spectral modelling, we estimated the hardness ratio (HR – defined as the ratio of 2–10 and 0.3–2 keV flux) and the spectral index for all the *Swift*/XRT observations. The HR (see the lower plot of the left panel of Fig. 4) and spectral index (upper plot of the left panel of Fig. 4) remain roughly constant at around 0.2 and 2, respectively. This indicates the soft nature of the X-ray emission. These results are consistent with the findings of Hinkle et al. (2022). The X-ray emission from AT2020ohl was completely power-law-dominated and plausibly generated through non-thermal processes, while as described in Sections 5.1 and 5.3 the UV-optical photons were produced due to blackbody emission. This is also evident from the uncorrelated nature of X-ray and UV-optical light curves.

4.3 Optical spectra

The spectral evolution of the transient in optical wavelength is shown in Fig. 5 along with the SDSS pre-transient spectrum of the host. From the upper panel of Fig. 5, it is clear that during its entire evolution (which corresponds to a time-scale of ∼500 d post disruption in the rest frame), no new line was produced due to the transient activity. This may rule out the possibility of a TDE or SN as the origin of AT2020ohl (see Section 5). As shown in the middle and bottom panels, the +68d spectrum of the transient(+ host) can be reproduced by adding a blackbody component to the host spectrum, where the blackbody emission is produced by a photosphere with a radius of $R_{68} \sim 3.1 \times 10^{15}$ cm and having an effective temperature $T_{68} = 8966 \pm 50$ K. Similarly, the +160d spectrum of the transient(+ host) can be reproduced by adding a blackbody component with $R_{160} \sim 1.9 \times 10^{15}$ cm and $T_{160} = 9100 \pm 115$ K to the host spectrum.[25] Therefore, the optical emission produced by the transient had a blackbody origin, and the nature of the source did not change appreciably during the first 200 d. Later the emitter became cooler, and slowly the transient intensity started to decline (see the bolometric light curve in Section 5).

4.4 Evolution in radio-band – connection with X-ray

As described in Section 2.2, the transient was detected in the JVLA *X* and *C* bands, at two epochs separated by 7 months. The radio

[25]Noteworthy, the resolution of SDSS spectrum is comparable to that of the observed spectra of the transient. To perform the fitting, we first calculated the flux values of every observed spectrum at the wavelength bins of the SDSS spectrum using cubic spline interpolation. Further, we added a blackbody component with the SDSS spectrum and fitted it to individual observed spectrum using `LMFIT` package by implementing χ^2 minimization technique while varying the radius and temperature of the blackbody.

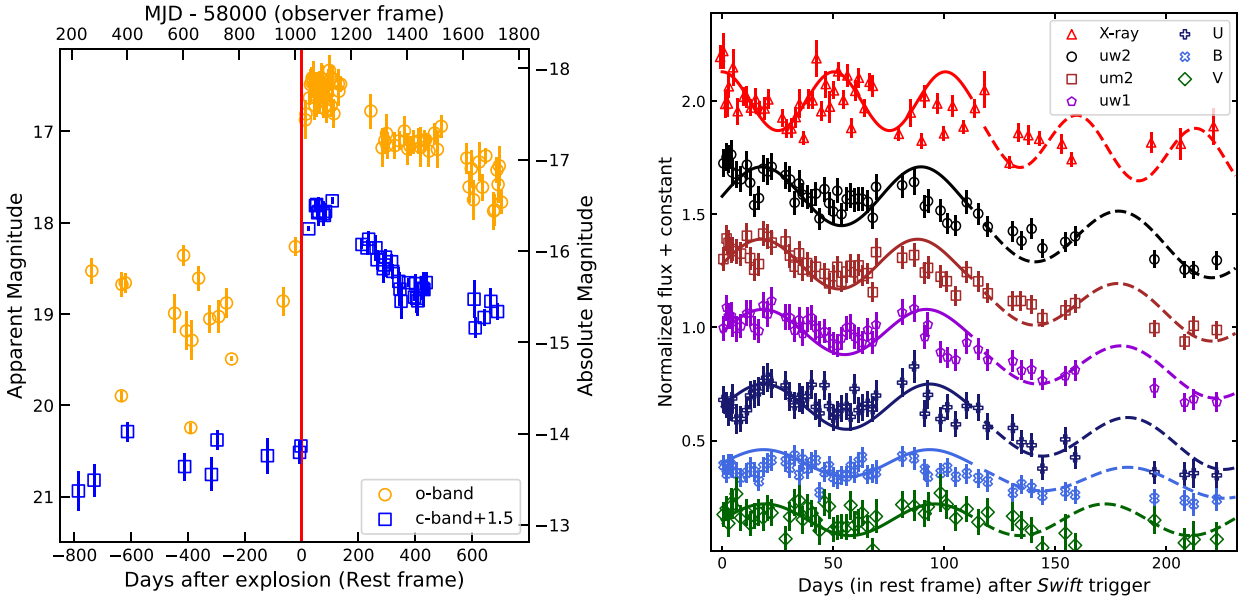

Figure 3. The X-ray, UV, and optical emission from AT2020ohl. The left panel shows the light curves of AT2020ohl in ATLAS o and c bands. The right panel shows only the early part (post-maximum) of the light curve observed from *Swift*. Significant variations in X-ray, and UV-optical light curves of the transient are noticeable. The solid and dashed lines overplotted with the data highlight the variation of flux (qualitatively) at the early and late phases after the maximum, respectively.

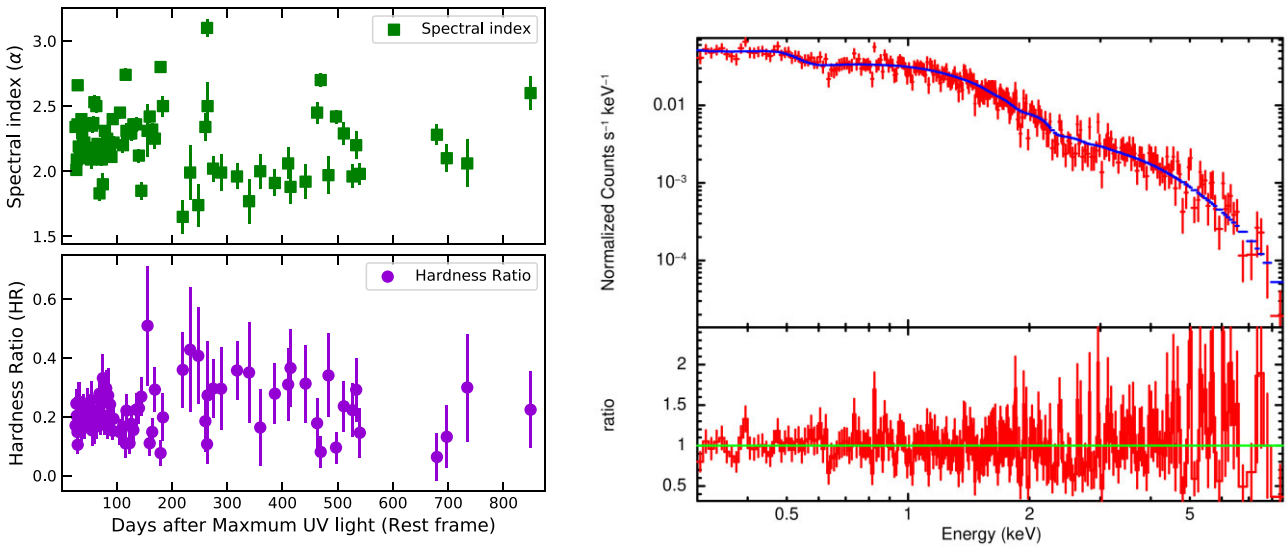

Figure 4. The left panel shows the variation of hardness ratio (HR) and spectral index (α) of the X-ray emission from the source during its evolution. The right panel shows the average X-ray spectrum of the transient during its evolution in first 100 d. See the text for the detail.

flux contours superimposed on the SDSS optical image for these two observations are shown in Fig. 6. The *X*-band observation in the higher resolution under B-array configuration (synthesized beamwidth $\theta = 0.6$ arcsec) resolves the central emission (O) from the nearby radio knot 'K' to the 1.5 arcsec north-east, as well as the nearby galaxy with compact radio emission ∼16 arcsec to the south and marked as 'G'. The integrated *X*-band flux density of the central core on +111 d is 33.5 ± 3.7 μJy. The corresponding measurement for the knot (K) is 18.4 ± 3.7 μJy.

Although the event was X-ray-luminous, the transient cannot be well localized due to the low resolution of the *Swift*/XRT (18 arcsec at 1.5 keV). To localize the X-ray transient, we observed it with *Chandra*/HRC-I. The upper right inset shows the central region, and the centroid of the X-ray source is consistent with the location of the central radio counterpart, confirming the nuclear-origin of AT2020ohl, and that the nearby radio-knot is not associated with the present transient activity (see Section 5).

The lower resolution D-array *X*-band images ($\theta = 7.2$ arcsec) could resolve the emission of NGC6297 (O + K) from the nearby galaxy G (see the green dot–dashed contour), but cannot the emission from the centre of the host. The integrated X-ray flux density in the D-array data is 65.08 ± 14 μJy. Since the nearby knot is not associated with the transient activity, its X-band luminosity is expected to be constant and we can conclude the transient *X*-band flux had been increased

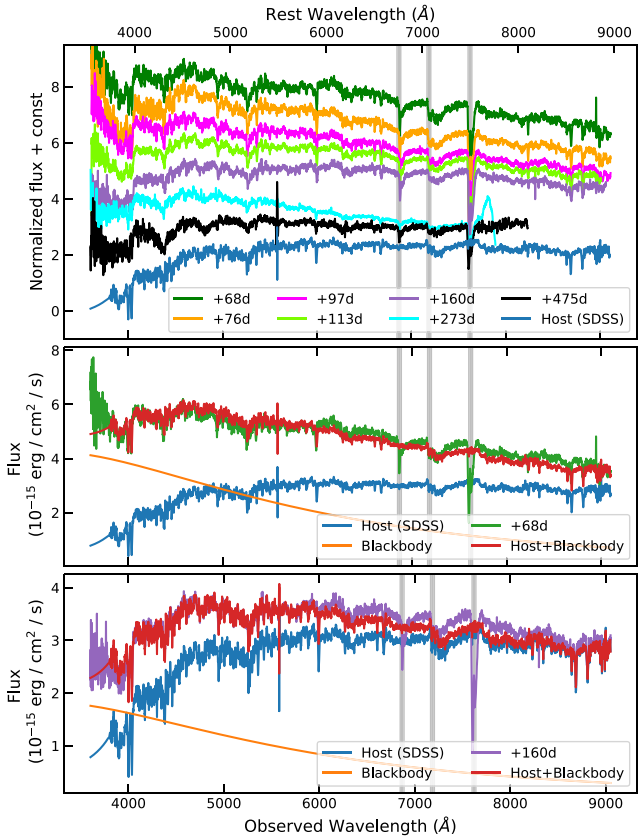

Figure 5. Spectroscopic evolution of AT2020ohl. The upper panel shows the spectra of the transient observed at +68d, +76d, +97d, +113d, +160d, +273d, and +475d. The SDSS spectrum of the host galaxy has also been shown. Over a time-scale of ∼500 d after the onset of the event, no strong line due to a TDE-like event has been observed. The narrow vertical grey regions mark the positions of teluric lines. The middle and bottom panels demonstrate the fitting of the Blackbody spectrum at two different epochs (+68d and +160d). The addition of the Blackbody spectrum (characterized by a single temperature 'T') emitted by a spherical region of radius 'R', with the host spectrum, can reproduce the transient spectrum at that epoch. For the +68d optical spectrum, the temperature and radius are, respectively, $T_{68} = 8966 \pm 50$K and $R_{68} \sim 3.1 \times 10^{15}$ cm, whereas the +160d spectrum can be reproduced with a blackbody surface at $T_{160} = 9100 \pm 115$ K and $R_{160} \sim 1.9 \times 10^{15}$ cm. These show there is not much evolution of the transient between these two epochs. The implication of this analysis has been discussed in Section 5.

to ∼47 ± 14.7 μJy by +313 d. This is nearly 1.4 times higher than the X-band flux of the transient at +111 d, although the two values are consistent given their errors. This shows that over 200 d of evolution, there was no significant change in the *X*-band luminosity of AT2020ohl. On the other hand, the D-array *C*-band observation ($\theta = 12$ arcsec) on +318 d could resolve none of the three sources and therefore gives only the upper limit on the flux of the transient (see the magenta dashed contour). The integrated flux density of the entire *C*-band contour shown in the figure is 132.78 ± 20 μJy. It is also noticeable from this image that the centroid of this contour coincides with the position of the nearby galaxy (G). It implies that G mostly dominates the radio flux. The peak flux density of this contour is 101.41 ± 10 μJy beam^{-1}. Therefore the upper limit of the central (i.e. transient) *C*-band flux of NGC6297 is roughly 30 μJy on +318 d (we consider it as the upper limit as this flux is a combination of transient flux and that of the radio-knot in *C* band).

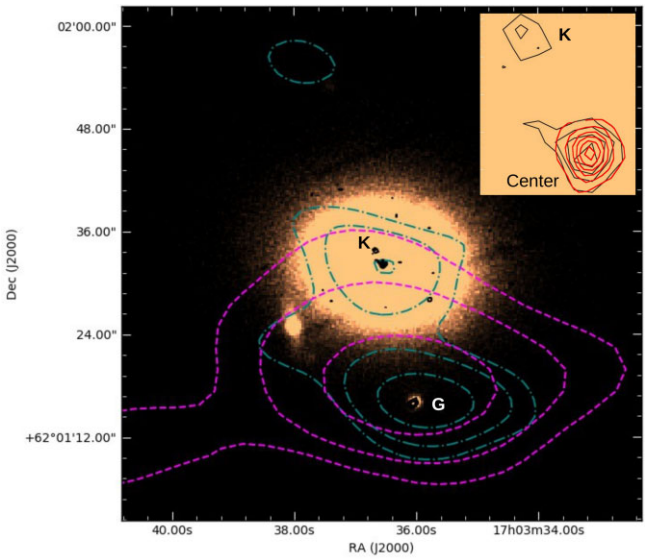

Figure 6. This figure shows the JVLA radio and *Chandra* X-ray counterparts of AT2020ohl, superposed on the archival optical image of the host (the bright big galaxy at the centre) taken from the PanSTARR survey (north is up and east is in the left direction). The JVLA *X*-band (B-array) contours (black) show the compact radio component distinguishing the centre (O), nearby knot (K) in the north-east, and the nearby compact radio source 'G'. The central region has been magnified in the inset where *Chandra* X-ray counterpart (in red) has also been shown. The green dot–dashed contours show the JVLA *X*-band (D-array) observations, while the magenta dashed contours show the JVLA *C*-band (D-array) observations. The *X*-band B array contours have been plotted at 3σ [1, 1.5, 2, 2.5], where the rms noise is $\sigma = 3$ μJy beam^{-1}. For the *X*-band D array also, the contours have been plotted at 3σ [1, 2, 4], where the rms noise is $\sigma = 6$ μJy beam^{-1}. For the *C*-band D array contours have been plotted at 3σ [1, 2, 4], where the rms noise is $\sigma = 5$ μJy beam^{-1}.

5 DISCUSSION AND CONCLUSIONS

Hinkle et al. (2022) pointed out that AT2020ohl/ASASSN-20hx simultaneously exhibited the characteristics of TDEs and AGN. Substantial emission in NUV, the smooth rise of the *TESS* light curve in *TESS* band, and the overall UV/optical evolution make the object comparable to TDE-like events. On the other hand, the linear rise of the flux and the absence of emission lines (also described in Section 4.3) differentiate AT2020ohl from canonical TDEs. Moreover, the non-thermal origin of the X-ray and the location of NGC6297 in the NIR colour–colour diagram are pieces of evidence for a possible AGN-origin of this event (also see Auchettl, Ramirez-Ruiz & Guillochon 2018), although strong AGN lines were absent until the +483d spectrum (see Fig. 5, and also Hinkle et al. 2022). In this work, we have revisited this problem to understand the origin of AT2020ohl using multiwavelength data. This is also to explore the probable mechanisms behind some of the ANTs.

5.1 The nature of NUV and optical radiation

Although the rise of AT2020ohl was smooth (a monotonic function of time, Hinkle et al. 2022), its post-maximum evolution in different UV-optical bands were significantly different from those of canonical stellar disruptions (see Section 4.1). The *Swift* NUV/optical light curves showed quasi-periodicity for nearly 120 d after the maximum (lower panel of Fig. 2). This indicates that the origin of these photons is roughly the same (although not precisely as discussed below).

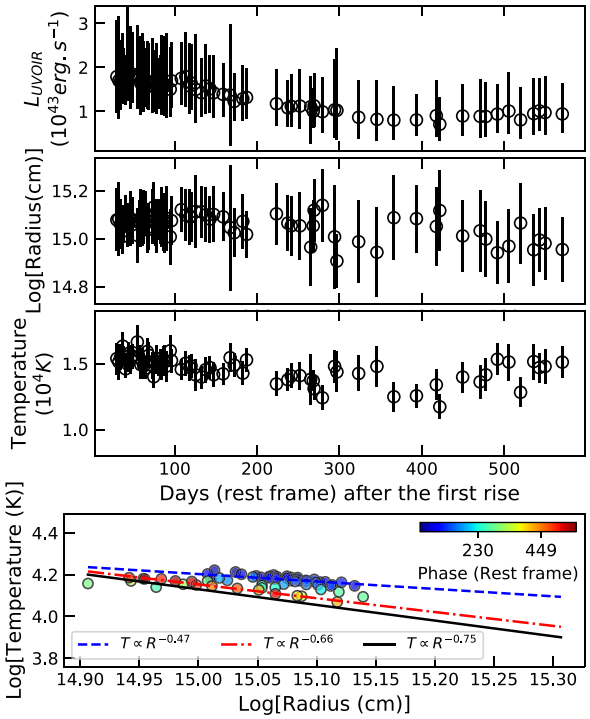

Figure 7. The UVOIR bolometric light curve of AT2020ohl. From top, the first, second, and third panels, respectively, describe the temporal evolution of bolometric luminosity (L_{UVOIR}), radius of the emitting surface, and its temperature. The lower most panel shows the observed variation of temperature with radius. The colour-bar indicates the phase in rest frame. The blue dashed line is fit to the data having phase value <200 d in rest frame showing $T \propto R^{-0.47}$. The red dot–dashed line is fit to the data having phase value >400 d in the rest frame showing $T \propto R^{-0.66}$. The black solid line shows the classical temperature–radius relation for an accretion disc ($T \propto R^{-3/4}$).

The upper panel of Fig. 7 shows the UV/optical bolometric light curve of the object along with the variation of the photospheric radius and temperature of the transient. To compute the bolometric light curve, we used the host-subtracted photometry of the transient obtained from the UVOT and ATLAS observations. The light curve was computed at the epochs of the *Swift* observations, and the observations from ATLAS were linearly interpolated to the *Swift* epochs. The observed SED of every epoch can be explained with a single blackbody. The temporal variation of blackbody radius and temperature have been shown in the second and third panels of the Fig. 7. Although the peak luminosity is consistent with canonical SNe, or TDEs, the post-peak decline rate is extremely shallow – maintaining a power law with temporal index ~ -0.07 during the first 120 d, and thereafter a steeper index of ~ -0.3 has been observed (where the negative sign indicates a decrease in flux with time, Section 4.1). Among nuclear transients, similar slow bolometric evolution has been observed in a few cases like ASASSN-17cv, ASASSN-18el (Trakhtenbrot et al. 2019a, b), and ASASSN-18jd (Neustadt et al. 2020). All these are ambiguous transients – either changing-look AGN (ASASSN-18el) or rejuvenated SMBH (ASASSN-17cv), or some unknown SMBH-driven transient in an AGN system (ASASSN-18jd).

The temperature obtained from the spectra are relatively lower than that computed from the SED-fitting (however, it is not an order of magnitude higher). This is mainly because SED contains spectral information over a larger wavelength range, and the photometric flux calibrations are better than spectroscopic flux calibrations. The higher value of inferred temperature while using the UV-optical photometry was noticed previously as well in nuclear transients like TDEs (e.g. ASASSN-14ae, Holoien et al. 2014). One probable reason may be that although we are assuming the origin of UV-optical photons is the same, actually UV photons are coming from the relatively inner hotter part of the disc, while the optical photons are generated at the relatively outer cooler part of the disc. The temperatures computed from the optical spectra are therefore lower than that calculated from the UV-dominated SED. Noteworthy, our last optical spectrum was taken on +475 d. So, at late-epoch, when UV is relatively less dominant, the photometric results become more consistent with spectroscopic results. However, beyond +475 d, we could only compute blackbody temperature and radius from photometric measurements. Therefore, with the existing data set, it is not possible to compare the results from photometry and spectroscopy beyond +475 d. Important information about the emitter of UV-optical radiation can be drawn from the correlation of temperature with radius shown in the fourth panel of the figure. In the early evolutionary phases (<200 d in rest frame), the radius (R) and temperature (T) follow the relation $T \propto R^{-0.47}$ (blue dash line), while in the later phases (>400 d in rest frame), they follow the relation $T \propto R^{-0.66}$ (red dot–dashed line). The black solid line shows the radius–temperature relation for a standard accretion disc ($T \propto R^{-3/4}$, Shakura & Sunyaev 1973). The transition of the radius–temperature relation from the shallower slope at the early epoch towards the standard accretion disc scenario at the late epoch essentially demonstrates that UV-optical emitting region has an accretion-disc like structure, which was initially evolving dynamically (just after the event), settled down with time, and approached to a steady accretion disc in due course of time.

5.2 Origin of X-ray and radio photons

Due to the quasi-simultaneous, high-resolution X-ray and radio observations, it is clear that the X-ray and radio emissions originate from the same location. Fig. 8 shows the nature of radio emission from the central component shown in Fig. 6. The left panel of Fig. 8 shows the post-disruption temporal evolution of the *X*-band radio luminosity between days $\sim$111 and $\sim$313. It also shows the upper limit of the *C*-band radio luminosity at 313 d and compares it to the 5 GHz radio luminosities of other transients (adopted from Alexander et al. 2020) like TDEs, radio-luminous SNe, and the central radio luminosities of Seyfert galaxies and radio-quiet AGNs. Clearly, AT2020ohl is several orders of magnitude fainter than other radio transients. As shown in the figure, the *X*-band luminosity of AT2020ohl increased only by 1.3 order in 200 d. This evolutionary rate is much slower than that of the other radio TDEs shown in the figure. At +313 d post-disruption, it was 10 times dimmer than the central radio luminosity of low-luminous Seyfert galaxies and low-luminous radio-quiet AGNs. At a similar phase of evolution, its radio luminosity is comparable only with some of the low-luminosity radio SNe. However, it had no other signature that suggests it could be an SN. Given its spectral properties at other wavelengths, particularly in the optical and NUV, we rule out the possibility of the association of AT2020ohl with any stellar explosion or disruption phenomenon – it is neither an SN nor a TDE. Nevertheless, the gradual increase of its high-frequency radio luminosity marks the possible slow emergence of an outflow from the centre of NGC6297.

The normalized radio spectra of AT2020ohl are compared with some of the radio-luminous TDEs in the right panel of Fig. 8. Here, the cyan and blue points are the *X*-band luminosities of the

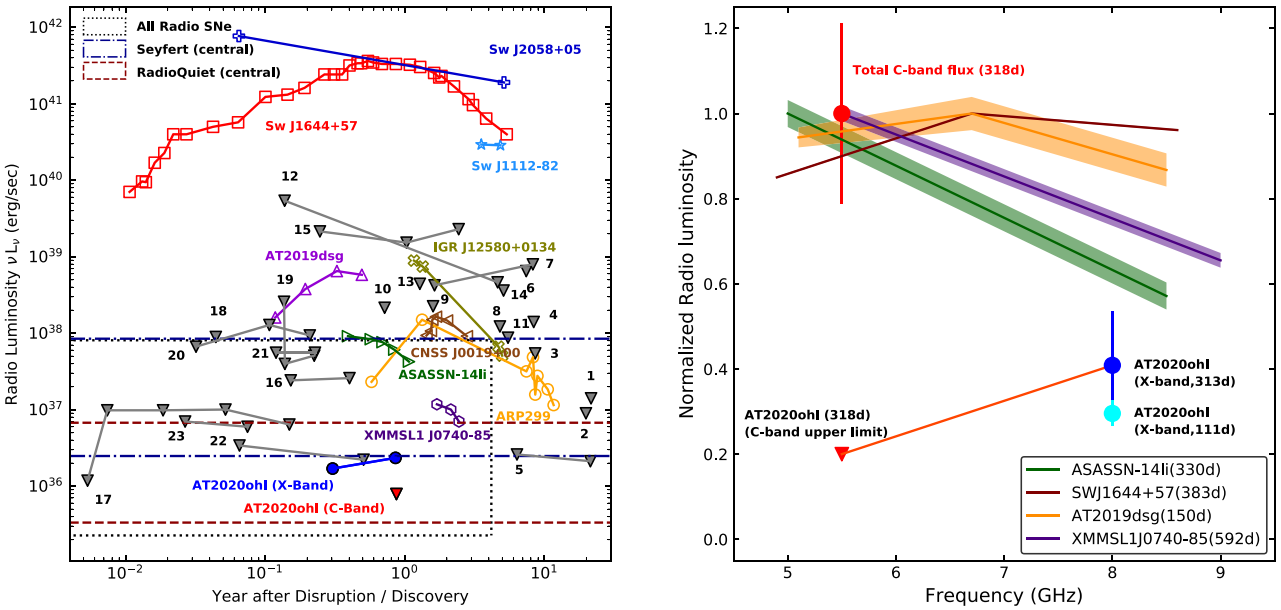

Figure 8. Evolution of AT2020ohl in radio band. The left panel shows the light curve and its comparison with other energetic sources, viz. radio counterparts of SNe (region marked with dotted line), emission from the central part of Syefert galaxy (region marked with dot–dashed line), and central radio luminosity of radio-quiet AGNs (region marked with dashed line), and radio TDEs (other points). The figure has been adopted from Alexander et al. (2020) and further modified. The downward grey triangles are showing upper limits of the fluxes of several TDEs which have been labelled with numbers as per first column of table 2 of Alexander et al. (2020). The right panel shows the comparison of radio spectra of AT2020ohl with the radio-spectra of some radio luminous TDEs at comparable (and late) epochs, viz. SWJ1644+57 (Zauderer et al. 2013), ASASSN-14li, XMMSL1 J0740-85 (Alexander et al. 2016, 2017), and AT2019dsg (Cannizzaro et al. 2021).

transient at +111 and +313 d, respectively. The red-filled circle corresponds to the total integrated flux in *C* band, and the downward triangle represents the upper limit of the C-band transient flux (see Section 4.4). The orange straight line (between the *C*-band upper limit and the *X*-band detection) shows the radio SED of the transient at ∼300 d after the disruption. The positive value of the spectral index (assuming $F \propto \nu^{\beta}$) shows it is in the optically thick phase at this stage of its evolution. The radio SED of AT2020ohl is also compared with the SEDs of the radio luminous TDEs observed at comparable epochs – SWJ164449.3+573451 (at +383d, Zauderer et al. 2013), XMMSL1J0740-85 (+ 592d, Alexander et al. 2017), ASASSN-14li (+330d, Alexander et al. 2016), and AT2019dsg (+ 150d, Cannizzaro et al. 2021). Unlike AT2020ohl, the other radio luminous TDEs became optically thin at these radio frequencies by 300 d after the peak. This radio characteristic of AT2020ohl distinguishes it from the canonical radio luminous TDEs, and in fact, advocates its non-TDE origin.

5.3 The combined picture

From multiwavelength analysis, it was well established that AT2020ohl was a slowly evolving transient. To understand the characteristic of its emission, the SED of the object has been modelled using multiwavelength broad-band data. In this regard, we used the *X*-band and *C*-band radio data of the transient observed on +318 d, along with the X-ray data from *Swift*/XRT, and host-subtracted NUV-optical data from *Swift*/UVOT observed on the +322 d (observations are quasi-simultaneous). The redshift-corrected observed broad-band SED is shown in Fig. 9 (see the upper right panel). We modelled the broad-band SED using the 'Jets SED modeller and fitting Tool' (JetSeT, Massaro et al. 2006; Tramacere et al. 2009; Tramacere, Massaro & Taylor 2011; Tramacere 2020). It is important to note that the host of AT2020ohl is an S0 galaxy. It had a mild pre-transient X-ray emission, showing mild AGN activity. It also does not have any star-forming lines in its spectrum (Section 3). The log of the ratio of its axes (i.e. major axis/minor axis) is *logr25*[26] = 0.16 ± 0.05 (Makarov et al. 2014), showing that it is a nearly face-on galaxy. Since the host is a mildly active galaxy, we consider that there is neither a torus nor a narrow/broad-line regions surrounding the SMBH. This is also consistent with the spectra of the host.

The observed SED is modelled assuming a very simple geometry of the system. During the transient activity, we assume a temporary accretion disc is produced (or there was already a disc-like structure present in this system). This is the origin of the blackbody radiation, which peaks in UV wavelength and maintains a constant disc temperature. The overall geometry of the system is Blazar-like, without the presence of a torus and narrow and broad line-forming regions. The non-thermal radiation is produced by a spherical homogeneous blob of leptonic plasma ($e^{\pm}$) entangled with magnetic fields, and it is moving along the jet, which is perpendicular to the plane of the disc. In the JetSeT environment, the system has a non-rotating SMBH of mass M_{BH} at its centre. Therefore, as described above, the components of the emitted broad-band spectrum are (1) a blackbody component produced by a Keplerian disc with an inner radius $R_{\rm in}$ and outer radius $R_{\rm out}$, respectively, having a disc luminosity $L_{\rm disc}$, and accretion efficiency $\alpha_{\rm eff}$; and (2) a non-thermal component, which is produced by the spherical blob having a radius *R* and at a distance $R_{\rm H}$ from the SMBH. The emitter density within the blob is n, the magnetic field is B, and the bulk Lorentz factor of its material is

[26]Here the length of each axis is the distance from the centre where surface brightness is reduced to 25 mag arcsec^{-2}.

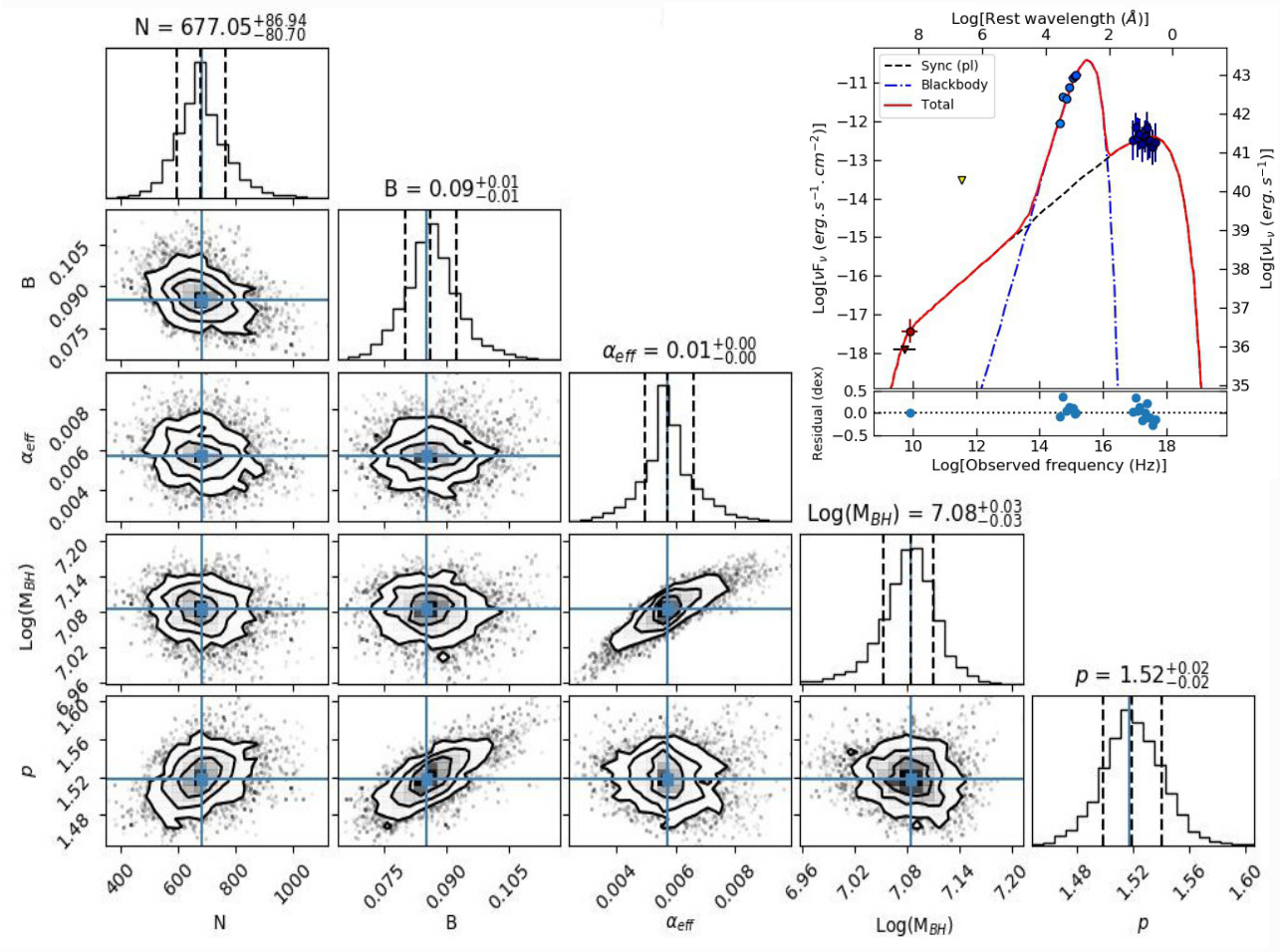

Figure 9. The broad-band SED modelling of AT2020ohl. X-ray and radio are produced from the synchrotron process, considering the single power-law model. However, the NUV-optical emission is mainly from the Blackbody radiation from the disc. The upper right inset shows the observed data points and different components of the model, along with their sum (in red) and residual. The corner plot shows the posterior distribution of five variables in the MCMC analysis.

Γ. The motion of the individual emission regions is random and entangled with the magnetic field, causing a spread in the Lorentz-factor between a minimum ($\gamma_{\rm min}$) and maximum ($\gamma_{\rm max}$). The energy distribution of the particles in the blob is assumed to be a power law (i.e. n(E) $\propto$ E^{-p}), and the jet points along a small angle θ with respect to the line of sight.

Table 1 summarizes the initial and final fitted values of the parameters. Since the redshift is well constrained its value is fixed. Given the limited number of constraints, we have also frozen several other parameters in this fitting process. We explored the number density of the emitter (n), the power-law index (p) of the synchrotron-emitting plasma, the accretion efficiency ($\alpha_{\rm eff}$) of the disc, the mass of the black hole ($M_{\rm BH}$), and the flux density (B) of the magnetic field. The transient was more luminous in the NUV than the optical, indicating that the blackbody temperature is high and peaking at a lower wavelength. We fixed the L$_{\rm disc}$ at $\sim$10^{43} erg s^{-1} (which is consistent with the bolometric luminosity at comparable epoch) so that the blackbody emission from the disc peaks in the UV. We further assumed that a mildly relativistic outflow produces the non-thermal emission ($\Gamma \sim 2$) and the $\theta \sim 5^{\circ}$. The values of all the other parameters [viz. $\gamma_{\rm min}$, $\gamma_{\rm max}$, $R_{\rm in}/R_{\rm sh}$ (where $R_{\rm sh}$ is the 'Schwarzschild radius' of the SMBH), $R_{\rm out}/R_{\rm sh}$, R, and $R_{\rm H}$] are assumed to be consistent with their typical values for a blazer system. The priors (initial starting and fixed values) are tabulated in the first column of Table 1, and the best-fitting parameters (posteriors) and their errors are tabulated in column 5. The model SED is shown in Fig. 9, along with the posterior distribution of the parameters.

The non-thermal emission produced by the mild-relativistic outflow is synchrotron self-absorption dominated in the radio frequencies and is optically thick. However, it is optically thin at higher frequencies (e.g. X-ray). We have also searched for the Gamma-ray counterpart from the *FmildERMI* archive and nothing was detected, indicating the absence of inverse Comptonized photons. Thus the SED is consistent with a disc-like accretion along with a mild-relativistic outflow.

5.4 Probable origin of AT2020ohl

We rule out the possibility of associating stellar explosion or disruption phenomena with the transient event AT2020ohl/ASASSN-20hx from the multiwavelength analysis. The absence of any regular SN line in the spectra immediately dismisses a nuclear-SN origin of this event. The same argument is also primarily applicable to rejecting the possibility of a TDE.

The rate of the rise of AT2020ohl and its host's mass are not similar to those of canonical TDEs (Hinkle et al. 2022). On the other hand,

Table 1. Parameters of JetSeT model.

Parameter (unit)	Start value	Min value	Max value	Best-fitting value (error)
γ_{min}	10[a]	–	–	–
γ_{max}	5E+05[a]	–	–	–
N (cm^{-3})	1000	50	5000	683.35 (±330.76)
p	2.5	−10	+10	1.52 (±0.07)
R_{in}/R_{sh}	50[a]	–	–	–
R_{out}/R_{sh}	100[a]	–	–	–
α_{eff}	0.01	0.0	0.1	0.006 (±0.005)
M_{BH} ($M_{\odot}$)	1E+07	9E+06	1E+08	1.2E+07 (±3.9E+06)
L_{disc} (erg s^{-1})	1E+43[a]	–	–	–
R (cm)	9E+14[a]	–	–	–
R_H (cm)	1E+17[a]	–	–	–
B (Gauss)	0.1	0.05	0.5	0.08 (±0.02)
$\theta(^{\circ})$	5[a]	–	–	–
Γ	2[a]	–	–	–
z	0.1671[a]	–	–	–

Note. [a]Parameters, which are fixed, have only the 'Start values' (second column). The parameters being varied have a start value (second column) with minimum and maximum limits (third and fourth columns, respectively). The best-fitting values of these parameters are given in the fifth column.

as discussed in Section 4.1, between +120 and +400 d, the temporal decay index of the UV-optical light curve was -0.41 ± 0.02. A similar decay rate was also observed in the X-ray light curve, which is much flatter than the $t^{-5/3}$ law. These properties show that AT2020ohl is most likely not associated with a stellar disruption event under the gravity of SMBH.

Nevertheless, the combined disc-wind models of TDEs (Strubbe & Quataert 2009; Lodato & Rossi 2011) can explain the UV-optical light curves to some extent. According to these models, the bound matters of the star form disc, while the unbound debris form wind-like outflow, causing a relatively flatter post-maximum decay in NUV-optical luminosity, maintaining a nature of $t^{-5/12}$. Although this decay index is consistent with the observations of AT2020ohl, there are large differences between the observed and predicted X-ray luminosities and X-ray decay rates. While models predict a higher luminosity and roughly $t^{-5/3}$ decay law over a period of ∼1000 d after disruption, the observed X-ray luminosity of AT2020ohl was much less than the NUV luminosity, and the corresponding X-ray decay rate was flatter than $t^{-5/3}$ law. Moreover, the origin of the X-ray is thermal by the Lodato & Rossi (2011) model, whereas, in Section 5.3, we argued that it is completely non-thermal.

From the UV-optical bolometric light curve, the migration of the radius–temperature relation towards a steady disc condition (Section 5.1), and the multiband SED modelling (Section 5.3), it is now established that an optically thick thermally emitting accretion disc must be present in this system. The variation in the UV-optical light curves and the non-standard behaviour of the radius–temperature relation at the early phases may be a manifestation of a dynamically evolving accretion disc. Since the base of the jet is supposed to be connected with the inner accretion disc, a variation in the X-ray light curve is also expected, if it originates due to the reprocessing of accretion disc photons. However, as discussed in Section 5.3, the X-ray and NUV-optical photons may have different origin and a strong correlation between light curves in these wavebands is unexpected.

A deeper investigation, like high-resolution multiwavelength imaging, is required to probe the centre of NGC6297 and to understand the origin of such ANTs. It is noticeable that NGC6297 is an S0 galaxy which may be a post-merger remnant. The presence of an extended galaxy exponential disc profile in this system (Section 3) strengthens the post-merging scenario. The plausible existence of an LLAGN at the centre of the host further strengthens the existence of a mild-accretion disc around the SMBH, which is otherwise not luminous. It is possible that in long periodical intervals, this disc either gets an additional matter supply from its host or the disc is intervened by some other compact object (like a bare SMBH of a merger), causing a sudden accretion and flaring activity of the disc in the UV optical bands as well as an outflow, which is the origin of the non-thermal X-ray and radio emission. A similar possibility was studied in the BL-Lac object OJ287 based on its long-term optical light curve (e.g. Sillanpaa et al. 1988), radio VLBA observations (e.g. Agudo et al. 2012; Gómez et al. 2022), and observations in other wavebands. Recently, high spatial resolution (∼0.1 arcsec) observations of UGC4211 – a post-merger galaxy have revealed the existence of binary SMBH with separation of ∼230pc (Koss et al. 2023). Noteworthy, VLBI observations have confirmed the existence of binary SMBHs, where the separation between two compact objects is as less as 7.3 pc (e.g. Kharb, Lal & Merritt 2017 and references therein). Therefore, the existence of binary SMBH at the centre of NGC6297 cannot be ruled out, and certainly, high-spatial resolution observations are necessary to confirm this possibility.

In the JVLA B-array *X*-band radio image (Fig. 6), the knot observed in the north-east direction from the centre of the galaxy is at a projected angular separation of 1.5 arcsec, which corresponds to a distance of ∼265 pc (≡ 850 light-years), which implies that this knot is not causally related to AT2020ohl. Unfortunately, we could not obtain JVLA observations at other frequencies (preferably in the *C* band) with comparable spatial resolution so that the spectral index of the knot and therefore its age could be calculated. However, given that the *X*-band flux of the knot is comparable to that of the central emission (Section 4.4) if we assume that the knot was indeed associated with the central activity due to an event similar to AT2020ohl, it must happened more than 850 yr ago.

The transition between active and inactive galaxies and vice versa is not completely understood. Merging of galaxies may be a key process for transition from inactive to active state. Since S0-galaxies have gone through the merging process, the study of their central regions is important to probe the post-merger scenario. It will also shed light on the gas accumulation process at the centres of these systems. The discovery of AT2020ohl/ASASSN-20hx is an example in this regard. Although in this study we ruled out the association of

stellar explosion or disruption phenomena, we could not precisely point out whether the sudden supply of matter to the pre-existing accretion disc triggered the event or it is due to a close interaction with another SMBH which was already a part of a binary SMBH system at the centre of the host. Multiwavelength high-resolution imaging has been planned to probe this system in the near future.

ACKNOWLEDGEMENTS

We thank all the observers of the 2 m HCT (operated by the Indian Institute of Astrophysics), who kindly provided part of their observing time for the optical spectroscopic observations of this transient. We acknowledge the use of public data from the *Swift* data archive. This research has used data obtained from the Chandra Data Archive and the *Chandra* Source Catalog, and software provided by the *Chandra* X-ray Center (CXC) in the application packages CIAO and SHERPA. The National Radio Astronomy Observatory is a facility of the National Science Foundation operated under cooperative agreement by Associated Universities, Inc. This work has used the NASA Astrophysics Data System and the NASA/IPAC Extragalactic Database (NED) which is operated by Jet Propulsion Laboratory, California Institute of Technology, under contract with the National Aeronautics and Space Administration. RR acknowledges IUCAA for providing access to their High-Performance Computing (HPC) facility for the analysis of JVLA data. Manipal Centre for Natural Sciences, Centre of Excellence, Manipal Academy of Higher Education (MAHE) is acknowledged for facilities and support. SN acknowledges support by the Science & Engineering Research Board (SERB), a statutory body of Department of Science & Technology (DST), Government of India (SERB-SURE Grant, File Number: SUR/2022/003864). This work has used data from the Sloan Digital Sky Survey (SDSS). Funding for the Sloan Digital Sky Survey V has been provided by the Alfred P. Sloan Foundation, the Heising–Simons Foundation, the National Science Foundation, and the Participating Institutions. SDSS acknowledges support and resources from the Center for High-Performance Computing at the University of Utah. The SDSS web site is www.sdss.org. SDSS is managed by the Astrophysical Research Consortium for the Participating Institutions of the SDSS Collaboration, including the Carnegie Institution for Science, Chilean National Time Allocation Committee (CNTAC) ratified researchers, the Gotham Participation Group, Harvard University, Heidelberg University, The Johns Hopkins University, L'Ecole polytechnique fédérale de Lausanne (EPFL), Leibniz-Institut für Astrophysik Potsdam (AIP), Max-Planck-Institut für Astronomie (MPIA Heidelberg), Max-Planck-Institut für Extraterrestrische Physik (MPE), Nanjing University, National Astronomical Observatories of China (NAOC), New Mexico State University, The Ohio State University, Pennsylvania State University, Smithsonian Astrophysical Observatory, Space Telescope Science Institute (STScI), the Stellar Astrophysics Participation Group, Universidad Nacional Autónoma de México, University of Arizona, University of Colorado Boulder, University of Illinois at Urbana-Champaign, University of Toronto, University of Utah, University of Virginia, Yale University, and Yunnan University.

DATA AVAILABILITY

The data used in this article will be shared on request to the corresponding author. The VLA data underlying this article are available from the NRAO Science Data Archive (https://archive.nrao.edu/archive/advquery.jsp). The data obtained from *Swift* and *Chandra* underlying this article are available at HEASARC archive (https://heasarc.gsfc.nasa.gov/docs/archive.html). The data from ATLAS are available at ATLAS forced photometry archive (https://fallingstar-data.com/forcedphot/). The spectroscopic data obtained from HCT for this project will be shared on reasonable request to the corresponding author.

REFERENCES

Adelman-McCarthy J. K. et al., 2006, ApJS, 162, 38
Agudo I., Marscher A. P., Jorstad S. G., Gómez J. L., Perucho M., Piner B. G., Rioja M., Dodson R., 2012, ApJ, 747, 63
Alexander K. D., Berger E., Guillochon J., Zauderer B. A., Williams P. K. G., 2016, ApJ, 819, L25
Alexander K. D., Wieringa M. H., Berger E., Saxton R. D., Komossa S., 2017, ApJ, 837, 153
Alexander K. D., van Velzen S., Horesh A., Zauderer B. A., 2020, Space Sci. Rev., 216, 81
Auchettl K., Ramirez-Ruiz E., Guillochon J., 2018, ApJ, 852, 37
Barbon R., Benetti S., Rosino L., Cappellaro E., Turatto M., 1990, A&A, 237, 79
Becker R. H., White R. L., Helfand D. J., 1995, ApJ, 450, 559
Beckmann V., Shrader C. R., 2012, Active Galactic Nuclei. Wiley-VCH Verlag GmbH & Co. KgaA
Bellm E. C. et al., 2019, PASP, 131, 018002
Blanchard P. K. et al., 2017, ApJ, 843, 106
Brimacombe J. et al., 2020, Astron. Telegram, 13891, 1
Burrows D. N. et al., 2005, Space Sci. Rev., 120, 165
Cannizzaro G. et al., 2021, MNRAS, 504, 792
Condon J. J., Cotton W. D., Greisen E. W., Yin Q. F., Perley R. A., Taylor G. B., Broderick J. J., 1998, AJ, 115, 1693
Deeley S. et al., 2020, MNRAS, 498, 2372
Diaz J., Bekki K., Forbes D. A., Couch W. J., Drinkwater M. J., Deeley S., 2018, MNRAS, 477, 2030
Dong S. et al., 2016, Science, 351, 257
Drake A. J. et al., 2009, ApJ, 696, 870
Drake A. J. et al., 2011, ApJ, 735, 106
Evans P. A. et al., 2012, ApJS, 203, 28
Gehrels N. et al., 2004, ApJ, 611, 1005
Gezari S. et al., 2009, ApJ, 698, 1367
Graham A. W., Driver S. P., 2005, Publ. Astron. Soc. Aust., 22, 118
Gregory P. C., Scott W. K., Douglas K., Condon J. J., 1996, ApJS, 103, 427
Gómez J. L. et al., 2022, ApJ, 924, 122
Hamuy M., Suntzeff N. B., Heathcote S. R., Walker A. R., Gigoux P., Phillips M. M., 1994, PASP, 106, 566
Hills J. G., 1975, Nature, 254, 295
Hinkle J. T. et al., 2020, Astron. Telegram, 13893, 1
Hinkle J. T. et al., 2022, ApJ, 930, 12
Hodapp K. W. et al., 2004, Astron. Nachr., 325, 636
Holoien T. W. S. et al., 2014, MNRAS, 445, 3263
Holoien T. W. S. et al., 2022, ApJ, 933, 196
Kankare E. et al., 2017, Nat. Astron., 1, 865
Kharb P., Lal D. V., Merritt D., 2017, Nat. Astron., 1, 727
Komossa S., Bade N., 1999, A&A, 343, 775
Koornneef J., Bohlin R., Buser R., Horne K., Turnshek D., 1986, Highlights of Astronomy, Vol. 7. Cambridge University Press, p. 833
Koss M. J. et al., 2023, ApJ, 942, L24
Kriek M., van Dokkum P. G., Labbé I., Franx M., Illingworth G. D., Marchesini D., Quadri R. F., 2009, ApJ, 700, 221
LaMassa S. M. et al., 2015, ApJ, 800, 144
Lacy M. et al., 2020, PASP, 132, 035001
Laurikainen E., Salo H., Buta R., Knapen J. H., 2009, ApJ, 692, L34
Leloudas G. et al., 2016, Nat. Astron., 1, 0002
Lin D., 2020, Astron. Telegram, 13895, 1
Lodato G., Rossi E. M., 2011, MNRAS, 410, 359
Maeda Y. et al., 2002, ApJ, 570, 671
Makarov D., Prugniel P., Terekhova N., Courtois H., Vauglin I., 2014, A&A, 570, A13

Massaro E., Tramacere A., Perri M., Giommi P., Tosti G., 2006, A&A, 448, 861
Nandi S. et al., 2019, MNRAS, 486, 5158
Neustadt J. M. M. et al., 2020, MNRAS, 494, 2538
Padovani P. et al., 2017, A&AR, 25, 2
Phillips M. M. et al., 2013, ApJ, 779, 38
Poznanski D., Prochaska J. X., Bloom J. S., 2012, MNRAS, 426, 1465
Querejeta M., Eliche-Moral M. C., Tapia T., Borlaff A., Rodríguez-Pérez C., Zamorano J., Gallego J., 2015, A&A, 573, A78
Quilis V., Moore B., Bower R., 2000, Science, 288, 1617
Quimby R. M., 2006, PhD thesis, The University of Texas at Austin
Rau A. et al., 2009, PASP, 121, 1334
Rees M. J., 1988, Nature, 333, 523
Richmond M. W., Treffers R. R., Filippenko A. V., Paik Y., Leibundgut B., Schulman E., Cox C. V., 1994, AJ, 107, 1022
Ricker G. R. et al., 2015, J. Astron. Telesc. Instrum. Syst., 1, 014003
Schlafly E. F., Finkbeiner D. P., 2011, ApJ, 737, 103
Schoenmakers A. P., de Bruyn A. G., Röttgering H. J. A., van der Laan H., 2001, A&A, 374, 861
Shakura N. I., Sunyaev R. A., 1973, A&A, 24, 337
Shappee B. et al., 2014, in American Astronomical Society Meeting Abstracts #223. p. 236.03
Sillanpaa A., Haarala S., Valtonen M. J., Sundelius B., Byrd G. G., 1988, ApJ, 325, 628
Smee S. A. et al., 2013, AJ, 146, 32
Strubbe L. E., Quataert E., 2009, MNRAS, 400, 2070
Tonry J. L. et al., 2018, PASP, 130, 064505
Trakhtenbrot B. et al., 2019a, Nat. Astron., 3, 242
Trakhtenbrot B. et al., 2019b, ApJ, 883, 94
Tramacere A., 2020, Astrophysics Source Code Library, record ascl:2009.001
Tramacere A., Giommi P., Perri M., Verrecchia F., Tosti G., 2009, A&A, 501, 879
Tramacere A., Massaro E., Taylor A. M., 2011, ApJ, 739, 66
Turatto M., Benetti S., Cappellaro E., 2003, in Hillebrandt W., Leibundgut B., eds, Proc. ESO/MPA/MPE, From Twilight to Highlight: The Physics of Supernovae. Springer Verlag, Berlin, Heidelberg, p. 200
van Dokkum P. G., 2001, PASP, 113, 1420
Vinkó J. et al., 2015, ApJ, 798, 12
Vollmann K., Eversberg T., 2006, Astron. Nachr., 327, 862
Wright E. L., 2006, PASP, 118, 1711
Zauderer B. A., Berger E., Margutti R., Pooley G. G., Sari R., Soderberg A. M., Brunthaler A., Bietenholz M. F., 2013, ApJ, 767, 152

APPENDIX A: SOME EXTRA MATERIAL

Table A1. Journal of spectroscopic observations of AT2020ohl.

UT date (yy-mm-dd)	JD 2450000 +	Phase[a] (d)	Range μm	Telescope	Grating (gr mm^{-1})	Exposure (s)	S/N[b] (pix^{-1})	Slit width (arcsec)
2020-08-31	9093.14	+68	0.36–0.9	HCT/HFOSC2	GR7+GR8	2700/2700	45	1.5
2020-09-08	9100.11	+76	0.36–0.9	HCT/HFOSC2	GR7+GR8	2700/2700	43	1.5
2020-09-29	9122.11	+97	0.36–0.9	HCT/HFOSC2	GR7+GR8	2700/2700	34	1.5
2020-10-16	9138.70	+113	0.36–0.9	HCT/HFOSC2	GR7+GR8	2700/2700	34	1.5
2020-12-02	9186.05	+160	0.36–0.9	HCT/HFOSC2	GR7+GR8	2700/2700	35	1.5
2021-03-27	9301.30	+273	0.36–0.8	HCT/HFOSC2	GR7	2700	38	1.5
2021-10-19	9507.14	+475	0.36–0.8	HCT/HFOSC2	GR7	1800	35	1.5
2000-05-30[c]	1695	−7328	0.38–0.9	SDSS/SPEC2	Blue/Red	3600	48	3 (fibre/ID 485)

Notes. [a]With reference to the explosion epoch JD 2459023.3.
[b]At 0.6 μm.
[c]This epoch marks the pre-transient spectroscopic observation of the host by the SDSS survey.

Table A2. Log of radio observation of AT2020ohl[a] from JVLA in C (4-8 GHz) and X (8–12 GHz).

UT date (yy-mm-dd)	JD 2450000+	Phase[b] (d)	Frequency (GHz)	Array	Flux (μJy)	Flux error[c] (μJy)
2020-10-29	9152.46	+128	10 (X-band)	B	33.5	3.7
2021-05-19	9353.64	+330	10 (X-band)	D	47	14.7
2021-05-24	9358.63	+335	05 (C-band)	D	∼30	–

Notes. [a]Here, only the fluxes of the central emission from NGC6297 have been tabulated.
[b]With reference to the explosion epoch JD 2459023.3.
[c]The upper limit has no error bars.

Table A3. *Swift*/UVOT photometry of AT2020ohl[a].

UT date (yyyy-mm-dd)	JD (2450000 +)	Phase[b] (d)	*uw*2 (mag)	*um*2 (mag)	*uw*1 (mag)	*uuu* (mag)	*ubb* (mag)	*uvv* (mag)
2020-07-19	9049.68	+26	15.94 ± 0.06	16.00 ± 0.05	15.93 ± 0.05	15.62 ± 0.04	15.12 ± 0.04	14.61 ± 0.04
2020-07-20	9051.14	+27	15.92 ± 0.06	15.91 ± 0.05	15.85 ± 0.05	15.64 ± 0.04	15.15 ± 0.04	14.59 ± 0.04
2020-07-21	9052.02	+28	15.92 ± 0.06	15.92 ± 0.05	15.88 ± 0.05	15.66 ± 0.05	15.12 ± 0.04	14.64 ± 0.04
2020-07-22	9053.23	+29	15.90 ± 0.06	15.95 ± 0.06	15.88 ± 0.05	15.64 ± 0.05	15.12 ± 0.05	14.58 ± 0.05
2020-07-23	9053.66	+30	15.98 ± 0.06	15.95 ± 0.05	15.91 ± 0.05	15.62 ± 0.05	15.13 ± 0.04	14.58 ± 0.04
2020-07-25	9055.59	+32	15.99 ± 0.06	15.96 ± 0.05	15.93 ± 0.05	15.69 ± 0.05	15.15 ± 0.05	14.55 ± 0.05
2020-07-27	9057.72	+34	16.01 ± 0.06	15.97 ± 0.05	15.92 ± 0.05	15.69 ± 0.05	15.17 ± 0.04	14.62 ± 0.04
2020-07-29	9060.43	+37	15.95 ± 0.06	15.89 ± 0.05	15.87 ± 0.05	15.66 ± 0.05	15.15 ± 0.04	14.61 ± 0.04
2020-07-31	9061.90	+38	16.03 ± 0.06	15.99 ± 0.05	15.87 ± 0.05	15.61 ± 0.05	15.13 ± 0.04	14.64 ± 0.04
2020-08-02	9063.76	+40	16.14 ± 0.06	16.04 ± 0.05	15.93 ± 0.05	15.60 ± 0.05	15.15 ± 0.04	14.62 ± 0.04
2020-08-04	9065.94	+42	16.10 ± 0.06	16.02 ± 0.05	15.94 ± 0.05	15.59 ± 0.05	15.19 ± 0.04	14.61 ± 0.04
2020-08-06	9067.87	+44	15.97 ± 0.06	15.88 ± 0.05	15.84 ± 0.05	15.56 ± 0.05	15.13 ± 0.04	14.62 ± 0.04
2020-08-08	9070.03	+46	15.98 ± 0.06	15.90 ± 0.05	15.87 ± 0.05	15.55 ± 0.05	15.11 ± 0.04	14.59 ± 0.04
2020-08-10	9071.75	+48	15.96 ± 0.06	15.92 ± 0.05	15.82 ± 0.05	15.57 ± 0.05	15.10 ± 0.04	14.61 ± 0.04
2020-08-16	9078.14	+54	15.99 ± 0.06	15.92 ± 0.05	15.88 ± 0.05	15.57 ± 0.05	15.10 ± 0.04	14.69 ± 0.04
2020-08-18	9080.13	+56	16.01 ± 0.06	15.98 ± 0.05	15.89 ± 0.05	15.61 ± 0.05	15.13 ± 0.05	14.62 ± 0.05
2020-08-20	9082.29	+58	16.13 ± 0.06	16.03 ± 0.05	15.94 ± 0.05	15.64 ± 0.05	15.08 ± 0.04	14.58 ± 0.04
2020-08-22	9084.29	+60	16.03 ± 0.06	15.97 ± 0.05	15.89 ± 0.05	15.61 ± 0.05	15.16 ± 0.05	14.57 ± 0.04
2020-08-24	9085.98	+62	16.09 ± 0.06	16.04 ± 0.05	15.95 ± 0.05	15.62 ± 0.05	15.09 ± 0.04	14.63 ± 0.04
2020-08-26	9087.97	+64	16.10 ± 0.06	16.01 ± 0.05	15.90 ± 0.05	15.61 ± 0.05	15.13 ± 0.04	14.59 ± 0.04
2020-08-28	9090.09	+66	16.12 ± 0.06	16.05 ± 0.05	15.89 ± 0.05	15.57 ± 0.05	15.11 ± 0.04	14.61 ± 0.04
2020-08-30	9092.02	+68	16.08 ± 0.06	16.03 ± 0.05	15.93 ± 0.05	15.65 ± 0.05	15.10 ± 0.04	14.63 ± 0.04
2020-09-01	9093.68	+70	16.21 ± 0.06	–	15.95 ± 0.05	15.67 ± 0.05	15.24 ± 0.05	14.67 ± 0.05
2020-09-03	9095.96	+72	16.06 ± 0.06	16.06 ± 0.05	15.94 ± 0.05	15.57 ± 0.05	15.15 ± 0.04	14.57 ± 0.04
2020-09-05	9098.06	+74	16.13 ± 0.06	16.11 ± 0.05	15.97 ± 0.05	15.64 ± 0.05	15.12 ± 0.04	14.59 ± 0.04
2020-09-07	9099.94	+76	16.17 ± 0.06	16.08 ± 0.05	16.00 ± 0.05	15.68 ± 0.05	15.17 ± 0.04	14.66 ± 0.04
2020-09-09	9101.80	+78	16.07 ± 0.06	16.03 ± 0.05	16.01 ± 0.05	15.67 ± 0.05	15.18 ± 0.04	14.65 ± 0.04
2020-09-11	9103.73	+80	16.19 ± 0.06	16.10 ± 0.05	15.97 ± 0.05	15.65 ± 0.05	15.16 ± 0.04	14.65 ± 0.04
2020-09-13	9106.11	+82	16.11 ± 0.06	16.05 ± 0.05	15.93 ± 0.05	15.65 ± 0.05	15.17 ± 0.04	14.65 ± 0.04
2020-09-15	9107.94	+84	16.09 ± 0.06	16.03 ± 0.05	15.92 ± 0.05	15.68 ± 0.05	15.13 ± 0.05	14.58 ± 0.04
2020-09-17	9109.70	+86	16.11 ± 0.06	16.06 ± 0.05	15.97 ± 0.05	15.59 ± 0.05	15.15 ± 0.04	14.65 ± 0.05
2020-09-19	9111.56	+88	16.11 ± 0.06	16.02 ± 0.05	15.98 ± 0.05	15.66 ± 0.05	15.10 ± 0.04	14.64 ± 0.04
2020-09-20	9113.15	+89	16.11 ± 0.06	16.07 ± 0.05	16.00 ± 0.05	15.65 ± 0.05	15.08 ± 0.04	14.61 ± 0.04
2020-09-23	9115.77	+92	16.12 ± 0.06	16.06 ± 0.05	15.94 ± 0.05	15.64 ± 0.04	15.16 ± 0.04	14.65 ± 0.04
2020-09-25	9118.06	+94	16.21 ± 0.06	16.16 ± 0.05	15.99 ± 0.05	15.65 ± 0.05	15.15 ± 0.04	14.73 ± 0.04
2020-09-27	9119.56	+96	16.05 ± 0.06	15.96 ± 0.06	15.92 ± 0.06	15.61 ± 0.05	15.15 ± 0.05	14.62 ± 0.05
2020-10-08	9131.49	+108	16.04 ± 0.06	15.99 ± 0.05	15.86 ± 0.05	15.56 ± 0.05	15.08 ± 0.04	14.58 ± 0.04
2020-10-14	9136.96	+113	16.03 ± 0.06	15.98 ± 0.05	15.85 ± 0.05	15.51 ± 0.05	15.09 ± 0.05	14.59 ± 0.05
2020-10-19	9141.91	+118	16.15 ± 0.06	16.06 ± 0.05	15.97 ± 0.05	15.67 ± 0.05	15.13 ± 0.04	14.61 ± 0.04
2020-10-20	9143.34	+120	16.12 ± 0.06	16.04 ± 0.05	15.92 ± 0.05	15.60 ± 0.05	15.17 ± 0.05	14.59 ± 0.04
2020-10-26	9149.08	+125	16.17 ± 0.06	16.08 ± 0.05	16.04 ± 0.05	15.69 ± 0.04	15.15 ± 0.04	14.55 ± 0.06
2020-10-29	9152.16	+128	16.24 ± 0.06	16.10 ± 0.05	16.06 ± 0.05	15.65 ± 0.04	15.13 ± 0.04	14.58 ± 0.04
2020-11-02	9156.11	+132	16.25 ± 0.06	16.18 ± 0.05	16.08 ± 0.05	15.71 ± 0.05	15.17 ± 0.04	14.63 ± 0.04
2020-11-07	9161.11	+137	16.13 ± 0.06	16.06 ± 0.05	15.99 ± 0.05	15.64 ± 0.05	15.15 ± 0.04	14.60 ± 0.04
2020-11-12	9166.32	+143	16.19 ± 0.06	16.10 ± 0.05	16.03 ± 0.05	15.65 ± 0.05	15.17 ± 0.04	14.64 ± 0.04
2020-11-17	9170.71	+147	16.26 ± 0.06	16.16 ± 0.05	16.08 ± 0.05	15.72 ± 0.05	15.19 ± 0.05	14.61 ± 0.05
2020-11-28	9182.21	+158	16.28 ± 0.06	16.21 ± 0.05	16.08 ± 0.05	15.72 ± 0.05	15.24 ± 0.05	14.62 ± 0.05
2020-12-02	9186.16	+162	16.34 ± 0.06	16.20 ± 0.05	16.13 ± 0.05	15.78 ± 0.05	15.20 ± 0.04	14.65 ± 0.05
2020-12-07	9190.78	+167	16.27 ± 0.06	16.22 ± 0.05	16.12 ± 0.05	15.79 ± 0.05	15.22 ± 0.04	14.66 ± 0.04
2020-12-12	9195.72	+172	16.39 ± 0.06	16.30 ± 0.05	16.18 ± 0.05	15.89 ± 0.05	15.26 ± 0.04	14.72 ± 0.04
2020-12-22	9206.18	+182	16.35 ± 0.06	16.26 ± 0.06	16.16 ± 0.05	15.77 ± 0.05	15.24 ± 0.04	14.67 ± 0.06
2020-12-27	9210.70	+187	16.32 ± 0.06	16.22 ± 0.05	16.13 ± 0.05	15.84 ± 0.05	15.25 ± 0.04	14.72 ± 0.04
2021-02-01	9246.99	+223	16.47 ± 0.06	16.37 ± 0.05	16.22 ± 0.05	15.90 ± 0.05	15.27 ± 0.05	14.63 ± 0.05
2021-02-15	9260.84	+237	16.54 ± 0.06	16.46 ± 0.05	16.31 ± 0.06	15.91 ± 0.06	15.28 ± 0.05	14.71 ± 0.05
2021-02-19	9265.01	+241	16.54 ± 0.07	16.35 ± 0.06	16.29 ± 0.06	15.91 ± 0.06	15.30 ± 0.06	14.70 ± 0.06
2021-03-02	9275.56	+252	16.47 ± 0.06	16.38 ± 0.06	16.31 ± 0.06	15.92 ± 0.06	15.28 ± 0.06	14.70 ± 0.06
2021-03-15	9288.59	+265	16.52 ± 0.07	16.44 ± 0.06	16.53 ± 0.07	15.93 ± 0.07	15.35 ± 0.07	14.86 ± 0.08
2021-03-18	9291.70	+268	16.61 ± 0.06	16.55 ± 0.06	16.36 ± 0.06	15.95 ± 0.06	15.33 ± 0.05	14.73 ± 0.05
2021-03-19	9292.70	+269	16.53 ± 0.07	16.48 ± 0.06	16.27 ± 0.06	15.88 ± 0.06	15.24 ± 0.06	14.64 ± 0.06
2021-03-29	9302.79	+279	16.60 ± 0.06	16.58 ± 0.05	16.45 ± 0.05	15.92 ± 0.05	15.28 ± 0.05	14.67 ± 0.05
2021-04-13	9317.59	+294	16.71 ± 0.07	16.58 ± 0.06	16.47 ± 0.06	16.10 ± 0.06	15.34 ± 0.05	14.73 ± 0.06
2021-04-15	9320.43	+297	16.58 ± 0.07	16.47 ± 0.06	16.36 ± 0.07	16.13 ± 0.07	15.28 ± 0.06	14.86 ± 0.07
2021-05-12	9346.83	+323	16.76 ± 0.06	16.58 ± 0.05	16.50 ± 0.05	16.07 ± 0.05	15.29 ± 0.05	14.80 ± 0.05

Table A3 – *continued*

UT date (yyyy-mm-dd)	JD (2450000 +)	Phase[b] (d)	*uw*2 (mag)	*um*2 (mag)	*uw*1 (mag)	*uuu* (mag)	*ubb* (mag)	*uvv* (mag)
2021-06-03	9369.03	+345	16.74 ± 0.06	16.66 ± 0.06	16.57 ± 0.06	16.07 ± 0.06	15.35 ± 0.05	14.82 ± 0.05
2021-06-24	9389.56	+366	16.81 ± 0.07	16.47 ± 0.14	16.54 ± 0.06	16.16 ± 0.06	15.31 ± 0.05	14.72 ± 0.06
2021-07-21	9417.01	+393	16.85 ± 0.06	16.77 ± 0.05	16.56 ± 0.05	16.14 ± 0.05	15.32 ± 0.05	14.75 ± 0.05
2021-08-14	9441.12	+417	16.70 ± 0.06	16.59 ± 0.05	16.48 ± 0.05	16.07 ± 0.05	15.29 ± 0.04	14.73 ± 0.04
2021-08-18	9445.33	+422	16.99 ± 0.06	16.90 ± 0.05	16.71 ± 0.05	16.21 ± 0.05	15.35 ± 0.04	14.74 ± 0.04
2021-09-15	9473.10	+449	16.60 ± 0.06	16.63 ± 0.05	16.49 ± 0.05	16.07 ± 0.05	15.34 ± 0.04	14.77 ± 0.04
2021-10-06	9494.32	+471	16.65 ± 0.06	16.58 ± 0.05	16.51 ± 0.05	16.09 ± 0.05	15.32 ± 0.04	14.74 ± 0.04
2021-10-13	9501.18	+477	16.63 ± 0.06	16.60 ± 0.05	16.52 ± 0.05	16.05 ± 0.05	15.35 ± 0.04	14.77 ± 0.04
2021-10-27	9515.25	+491	16.61 ± 0.06	16.56 ± 0.05	16.42 ± 0.05	16.08 ± 0.05	15.35 ± 0.04	14.80 ± 0.04
2021-11-10	9529.21	+505	16.56 ± 0.06	16.48 ± 0.05	16.46 ± 0.05	16.15 ± 0.05	15.40 ± 0.04	14.77 ± 0.04
2021-11-24	9543.43	+520	16.76 ± 0.06	16.69 ± 0.05	16.58 ± 0.05	16.18 ± 0.05	15.37 ± 0.04	14.73 ± 0.04
2021-12-10	9559.38	+536	16.61 ± 0.06	16.48 ± 0.06	16.42 ± 0.05	16.10 ± 0.05	15.33 ± 0.04	14.80 ± 0.04
2021-12-17	9566.25	+542	16.50 ± 0.06	16.44 ± 0.05	16.38 ± 0.05	16.07 ± 0.05	15.37 ± 0.04	14.74 ± 0.04
2021-12-24	9573.14	+549	16.53 ± 0.06	16.46 ± 0.05	16.42 ± 0.05	16.11 ± 0.05	15.35 ± 0.04	14.77 ± 0.04
2021-12-31	9580.31	+557	16.56 ± 0.06	16.42 ± 0.05	16.37 ± 0.05	16.09 ± 0.05	15.36 ± 0.04	14.77 ± 0.04
2022-01-14	9594.09	+570	16.53 ± 0.06	16.52 ± 0.05	16.44 ± 0.05	16.14 ± 0.05	15.44 ± 0.05	14.77 ± 0.05
2022-04-17	9686.70	+663	16.87 ± 0.06	16.74 ± 0.06	16.69 ± 0.06	16.23 ± 0.05	–	–
2022-05-01	9701.48	+678	16.88 ± 0.06	16.77 ± 0.06	16.72 ± 0.06	16.22 ± 0.05	–	–
2022-05-05	9704.76	+681	16.96 ± 0.06	16.86 ± 0.06	16.77 ± 0.06	16.26 ± 0.05	–	–
2022-05-15	9714.80	+691	17.00 ± 0.06	16.93 ± 0.06	16.79 ± 0.05	16.31 ± 0.05	–	–
2022-05-29	9728.62	+705	17.05 ± 0.07	16.89 ± 0.07	16.75 ± 0.07	16.32 ± 0.06	–	–
2022-06-02	9732.86	+709	16.91 ± 0.06	16.83 ± 0.06	16.74 ± 0.06	16.36 ± 0.05	–	–
2022-06-15	9746.47	+723	17.22 ± 0.07	17.08 ± 0.07	16.93 ± 0.06	16.28 ± 0.05	–	–
2022-06-16	9746.94	+723	16.92 ± 0.06	16.85 ± 0.06	16.73 ± 0.06	16.29 ± 0.05	–	–
2022-06-26	9757.19	+733	16.84 ± 0.06	16.79 ± 0.06	16.67 ± 0.05	16.29 ± 0.05	–	–
2022-07-10	9771.00	+747	16.93 ± 0.06	16.86 ± 0.06	16.71 ± 0.05	16.23 ± 0.05	–	–

Notes. [a]The magnitude of the transient at different UVOT bands have been determined after subtracting the host flux at the transient location (see Section 3).
[b]With reference to the explosion epoch JD 2459023.3.

Table A4. *Swift*/XRT observations of AT2020ohl.

UT Date (yyyy-mm-dd)	JD (2450000+)	Flux (0.3–10 KeV) 10^{-12} erg cm^{-2} s^{-1}	Spectral Index[a]	Hardness Ratio[b]
2020-07-18	9049.178	3.23 ± 0.26	2.34 ± 0.12	0.170 ± 0.037
2020-07-20	9050.637	3.36 ± 0.39	2.01 ± 0.07	0.244 ± 0.048
2020-07-20	9051.486	2.19 ± 0.30	2.09 ± 0.11	0.203 ± 0.058
2020-07-22	9052.729	2.20 ± 0.30	2.36 ± 0.19	0.147 ± 0.057
2020-07-22	9053.161	2.58 ± 0.26	2.66 ± 0.15	0.104 ± 0.030
2020-07-24	9055.085	3.0 ± 0.40	2.19 ± 0.09	0.251 ± 0.067
2020-07-26	9057.217	2.03 ± 0.29	2.11 ± 0.19	0.236 ± 0.078
2020-07-29	9059.930	2.35 ± 0.20	2.40 ± 0.12	0.154 ± 0.036
2020-07-30	9061.398	2.34 ± 0.24	2.29 ± 0.21	0.210 ± 0.044
2020-08-01	9063.257	2.11 ± 0.18	2.36 ± 0.13	0.225 ± 0.050
2020-08-03	9065.447	2.30 ± 0.23	2.22 ± 0.13	0.170 ± 0.043
2020-08-05	9067.369	2.08 ± 0.17	2.18 ± 0.12	0.213 ± 0.046
2020-08-08	9069.530	2.09 ± 0.25	2.10 ± 0.18	0.196 ± 0.047
2020-08-09	9071.254	2.29 ± 0.22	2.18 ± 0.13	0.240 ± 0.056
2020-08-16	9077.643	1.89 ± 0.19	2.09 ± 0.14	0.256 ± 0.065
2020-08-18	9079.635	1.64 ± 0.20	2.35 ± 0.17	0.153 ± 0.054
2020-08-20	9081.791	1.65 ± 0.21	2.37 ± 0.26	0.195 ± 0.051
2020-08-22	9083.790	1.90 ± 0.23	2.53 ± 0.19	0.162 ± 0.054
2020-08-23	9085.484	2.20 ± 0.32	2.17 ± 0.10	0.187 ± 0.049
2020-08-25	9087.470	1.44 ± 0.15	2.50 ± 0.16	0.174 ± 0.050
2020-08-28	9089.595	2.30 ± 0.21	2.21 ± 0.13	0.198 ± 0.045
2020-08-30	9091.518	2.27 ± 0.19	2.10 ± 0.12	0.224 ± 0.047
2020-08-31	9093.277	3.2 ± 0.40	1.83 ± 0.09	0.278 ± 0.057
2020-09-02	9095.457	2.03 ± 0.22	2.12 ± 0.13	0.190 ± 0.049
2020-09-05	9097.555	2.63 ± 0.29	2.09 ± 0.09	0.249 ± 0.049
2020-09-06	9099.440	2.13 ± 0.35	1.90 ± 0.09	0.331 ± 0.080

Table A4 – *continued*

UT Date (yyyy-mm-dd)	JD (2450000+)	Flux (0.3–10 KeV) 10^{-12} erg cm^{-2} s^{-1}	Spectral Index[a]	Hardness Ratio[b]
2020-09-08	9101.299	2.49 ± 0.19	2.20 ± 0.11	0.204 ± 0.041
2020-09-10	9103.228	2.91 ± 0.20	2.31 ± 0.10	0.172 ± 0.033
2020-09-13	9105.609	2.28 ± 0.20	2.12 ± 0.11	0.296 ± 0.061
2020-09-14	9107.443	2.82 ± 0.25	2.25 ± 0.13	0.166 ± 0.042
2020-09-16	9109.202	1.66 ± 0.21	2.19 ± 0.18	0.272 ± 0.090
2020-09-18	9111.062	2.48 ± 0.23	2.16 ± 0.12	0.206 ± 0.044
2020-09-20	9112.653	2.77 ± 0.21	2.16 ± 0.11	0.242 ± 0.045
2020-09-22	9115.272	2.10 ± 0.19	2.11 ± 0.12	0.196 ± 0.040
2020-09-25	9117.563	2.68 ± 0.19	2.40 ± 0.10	0.151 ± 0.029
2020-09-26	9119.093	2.59 ± 0.24	2.22 ± 0.13	0.193 ± 0.046
2020-10-08	9130.991	1.53 ± 0.15	2.45 ± 0.16	0.147 ± 0.043
2020-10-13	9136.463	2.0 ± 0.30	2.2 ± 0.40	0.166 ± 0.059
2020-10-18	9141.403	1.38 ± 0.17	2.74 ± 0.21	0.108 ± 0.049
2020-10-20	9142.838	2.36 ± 0.25	2.31 ± 0.14	0.220 ± 0.055
2020-10-26	9148.575	2.20 ± 0.23	2.29 ± 0.14	0.109 ± 0.034
2020-10-29	9151.660	1.54 ± 0.16	2.29 ± 0.15	0.175 ± 0.056
2020-11-02	9155.616	2.15 ± 0.24	2.36 ± 0.19	0.154 ± 0.038
2020-11-07	9160.613	1.69 ± 0.15	2.36 ± 0.13	0.223 ± 0.055
2020-11-12	9165.822	2.10 ± 0.20	2.12 ± 0.13	0.229 ± 0.051
2020-11-16	9170.205	2.5 ± 0.40	1.85 ± 0.08	0.268 ± 0.065
2020-11-28	9181.680	0.89 ± 0.14	2.31 ± 0.21	0.509 ± 0.202
2020-12-02	9185.658	1.55 ± 0.20	2.42 ± 0.18	0.109 ± 0.042
2020-12-06	9190.274	1.50 ± 0.21	2.32 ± 0.12	0.148 ± 0.047
2020-12-11	9195.217	1.42 ± 0.16	2.25 ± 0.16	0.292 ± 0.075
2020-12-22	9205.675	1.31 ± 0.22	2.8 ± 0.50	0.076 ± 0.043
2020-12-26	9210.074	0.97 ± 0.16	2.5 ± 0.40	0.197 ± 0.080
2021-01-31	9246.490	1.34 ± 0.23	1.65 ± 0.17	0.359 ± 0.129
2021-02-14	9260.073	1.31 ± 0.35	1.99 ± 0.24	0.427 ± 0.210
2021-03-01	9275.065	1.70 ± 0.40	1.74 ± 0.26	0.407 ± 0.163
2021-03-14	9288.088	1.60 ± 0.40	2.34 ± 0.27	0.184 ± 0.104
2021-03-17	9291.205	0.92 ± 0.19	3.10 ± 0.70	0.106 ± 0.067
2021-03-18	9292.199	0.80 ± 0.19	2.50 ± 0.30	0.272 ± 0.182
2021-03-28	9302.290	1.28 ± 0.24	2.02 ± 0.15	0.295 ± 0.099
2021-04-12	9317.089	1.15 ± 0.20	1.99 ± 0.18	0.295 ± 0.140
2021-05-11	9346.298	1.59 ± 0.22	1.96 ± 0.17	0.357 ± 0.099
2021-06-03	9368.526	0.94 ± 0.23	1.77 ± 0.18	0.350 ± 0.170
2021-06-23	9389.054	0.80 ± 0.17	2.00 ± 0.21	0.163 ± 0.130
2021-07-20	9416.049	1.15 ± 0.21	1.91 ± 0.19	0.278 ± 0.102
2021-08-13	9440.422	0.77 ± 0.17	2.06 ± 0.20	0.309 ± 0.122
2021-08-18	9444.803	0.91 ± 0.14	1.88 ± 0.19	0.365 ± 0.131
2021-09-14	9472.473	0.70 ± 0.19	1.92 ± 0.22	0.312 ± 0.131
2021-10-06	9493.723	0.61 ± 0.09	2.45 ± 0.24	0.177 ± 0.084
2021-10-12	9500.419	0.77 ± 0.15	2.70 ± 0.50	0.080 ± 0.053
2021-10-27	9514.608	0.55 ± 0.12	1.97 ± 0.15	0.340 ± 0.142
2021-11-09	9528.471	0.73 ± 0.14	2.42 ± 0.28	0.095 ± 0.053
2021-11-24	9542.890	0.83 ± 0.12	2.29 ± 0.22	0.235 ± 0.086
2021-12-10	9558.810	0.96 ± 0.20	1.96 ± 0.22	0.222 ± 0.090
2021-12-17	9565.588	0.84 ± 0.07	2.20 ± 0.13	0.291 ± 0.107
2021-12-23	9572.402	0.88 ± 0.12	1.98 ± 0.17	0.145 ± 0.083
2021-12-31	9579.766	0.31 ± 0.09	1.90 ± 0.40	0.558 ± 0.374
2022-05-14	9714.201	0.60 ± 0.15	2.28 ± 0.16	0.063 ± 0.080
2022-06-01	9732.350	0.86 ± 0.35	2.10 ± 0.48	0.131 ± 0.106
2022-07-09	9770.021	0.41 ± 0.12	2.06 ± 0.21	0.299 ± 0.182
2022-11-03	9886.558	0.58 ± 0.14	2.60 ± 0.50	0.223 ± 0.129

Notes. [a]The spectral index (α) is defined by the formula $F_{Xray} \propto \nu^{\alpha}$.
[b]The hardness ratio (HR) is defined as the ratio of 2–10 keV and 0.3–2 keV flux.

This paper has been typeset from a TEX/LATEX file prepared by the author.